buildings

MDPI

Article

Explicit Method for the Simulation of the Out-of-Plane Collapse of Unreinforced Masonry Walls: Influence of Hourglass Control, Damping, and Element Formulation

Elesban Nochebuena-Mora * and Nuno Mendes *

Department of Civil Engineering, Institute for Sustainability and Innovation in Structural Engineering (ISISE), Advanced Production and Intelligent Systems (ARISE) Associated Laboratory, University of Minho, 4800-058 Guimaraes, Portugal

* Correspondence: enochemora@gmail.com (E.N.-M.); nunomendes@civil.uminho.pt (N.M.)

Abstract

Nonlinear dynamic FEM analyses of unreinforced masonry (URM) must address convergence difficulties in implicit solutions, conditional stability in explicit solutions, and numerical artifacts related to element integration. This study compares implicit and explicit time-integration procedures using a homogenised three-dimensional model of a dry-joint masonry specimen tested on a shake table. The influence of hourglass-control formulation and scale factor, artificial energy, Rayleigh damping coefficient β, linear bulk viscosity, and element formulation was assessed against the experimental displacement response. Before damage initiation, the hourglass-control formulations produced similar responses. After cracking, increasing the scale factor produced a stiffer response and delayed collapse. The selected formulations reproduced the global collapse mechanism with artificial-energy ratios between 5% and 7% during damage propagation and below 10% at collapse. The use of the full value of β or a linear bulk-viscosity parameter of 5.0 reduced the stable time increment by approximately seven times, and the models failed to reproduce the collapse. Under nonlinear conditions, the response was more sensitive to element formulation than to the time-integration procedure. When collapse occurred, the implicit analyses required approximately twice the computational time of the corresponding explicit analyses. The results provide preliminary guidance for explicit FEM simulations of URM.

Keywords: nonlinear dynamic analysis; energy balance; computational performance; numerical simulation; artificial energy; 3D FEM modelling

Check for updates

Academic Editor: Salvatore Verre

Received: 9 September 2026
Revised: 9 October 2026
Accepted: 15 October 2026
Published: 20 October 2026

Copyright: © 2026 by the authors. Licensee MDPI, Basel, Switzerland. This article is an open access article distributed under the terms and conditions of the Creative Commons Attribution (CC BY) license.

1. Introduction

Unreinforced masonry (URM) buildings are particularly vulnerable to seismic actions because of their low tensile strength, limited shear capacity, and sometimes the poor connections between structural components. The damage caused by earthquakes is associated with in-plane (IP) and out-of-plane (OOP) mechanisms. OOP mechanisms are especially critical because they are brittle and can lead to the early collapse of walls that are insufficiently connected to the rest of the structure [1]. Predicting the initiation and progression of these mechanisms remains challenging because the response depends on the heterogeneous and anisotropic behaviour of masonry, the interaction between structural components, and the characteristics of the seismic input [2].

Different numerical strategies have been developed to simulate the nonlinear response of masonry structures. Detailed micro-modelling can represent masonry units, joints, and

their interactions separately, whereas macro-modelling describes masonry as an equivalent continuum [3]. Discrete element methods (DEM) are well suited to problems governed by joint opening, sliding, impact, and the motion of individual units. However, explicitly representing the masonry arrangement can become computationally demanding for large buildings with complex geometries and irregular units [2]. Finite element method (FEM) models provide a simpler alternative when the global response of large structures is of primary interest. Since masonry is represented as a homogenised continuum, it cannot reproduce all local discontinuities or the movements of individual units [2]. A detailed review of these numerical strategies is provided in [2].

For URM, nonlinear dynamic (transient) analysis is especially challenging because masonry is a quasi-brittle, anisotropic, heterogeneous material with very low tensile strength, frictional shear behavior, and complex cyclic deterioration (cracking, crushing, tension/compression softening, shear transfer across cracks, stiffness and strength degradation) [2,4]. Nonlinear dynamic analysis of structures requires step-by-step time integration of the semi-discrete equations of motion obtained from the FEM spatial discretization. Time integration schemes are broadly divided into implicit and explicit families.

In implicit methods, the unknowns at the current time step appear on both sides of the discrete equations, so an effective stiffness matrix must be factorized and, in nonlinear analysis, iterative solution procedures such as Newton–Raphson must be carried out at every step. Material softening, stiffness degradation, contact, and large displacements can therefore increase the computational cost and lead to convergence difficulties [5,6]. These problems become particularly relevant when simulating quasi-brittle materials with very low tensile strength.

Explicit methods, by contrast, update the response using only quantities from previous steps; with a diagonal (lumped) mass matrix they require only vector operations, no matrix factorizations and no iterations [4,7,8]. Explicit integration is conditionally stable and requires a time increment smaller than the critical value associated with the smallest element dimension and the material wave speed. Consequently, explicit analyses may require a very large number of increments, particularly for fine meshes or stiff materials. The computational cost of each increment is approximately proportional to the size of the model. The time increment is only dependent on the element dimensions and material properties, not on the complexity of the analysis [9]. This makes explicit schemes particularly attractive for large, strongly nonlinear systems in which small time steps are in any case required by the physics of the problem (wave propagation, impact, progressive collapse) [7,8,10].

Explicit methods for FEM modelling have been applied extensively in fields such as metal forming, impact, and contact mechanics. In masonry buildings, they have also been used to study the structural response to blast loading [11–14]. Several studies have applied explicit solvers in DEM-based models for seismic assessments of URM buildings [15–23], whereas their application within FEM remains limited. Tarque et al. [24] used shell elements and an explicit solver to reproduce shake table tests on an adobe house. Nochebuena-Mora et al. [25] used plane-stress elements to investigate the IP response of masonry spandrels and assessed the influence of different numerical parameters on the solution. Yang [26] compared implicit and explicit solutions for a URM building and obtained similar nonlinear dynamic responses. Noor-E-Khuda [27] investigated the OOP behaviour of masonry walls with different openings and boundary conditions, although the analyses were performed under incrementally applied lateral loading (nonlinear pushover analysis). Mouzakis and Carydis [4] developed a smeared-crack macromodel for the in-plane cyclic response of URM walls and implemented it in Abaqus/Explicit.

FEM modelling also requires careful consideration of the spatial discretisation. Linear elements with full integration may exhibit shear locking under bending, whereas reduced

integration can introduce hourglass (zero-energy) modes [28–30]. Artificial forces are required to suppress these zero-energy deformation modes, but they generate artificial energy and may modify the structural response. Their magnitude depends on the hourglass-control formulation and user-defined parameters. Furthermore, in explicit solvers, damping introduced to control the high-frequency response may affect both the stable time increment and the predicted damage or collapse mechanism.

Despite their relevance, the effects of hourglass control, artificial energy, high-frequency damping, and element formulation have received limited attention in explicit FEM analyses of URM structures. In particular, suitable levels of artificial energy have not been established for simulations involving the progressive damage and collapse of quasi-brittle materials. Previous studies applying the explicit solver to masonry have not examined the influence of these numerical parameters. In Nochebuena-Mora et al. [25], an artificial-energy limit of 10% was adopted based on [31], without evaluating its suitability for URM. Moreover, that study considered simple two-dimensional geometries modelled using shell elements. In three-dimensional models, where more complex deformation modes may develop, the applicability of this limit remains uncertain. The computational implications of these parameters and their influence on comparisons between implicit and explicit solutions also remain insufficiently examined.

This study investigates these aspects using a homogenised three-dimensional FEM model of a dry joint masonry specimen tested on a shake table. The negligible tensile capacity of the dry joints led to a highly nonlinear response characterised by joint opening, rocking, stiffness degradation, large displacements, and collapse. The specimen therefore provided a suitable reference for comparing the implicit and explicit procedures under severe nonlinear conditions. Although the homogenised model could not reproduce the movement of individual masonry units, it allowed the influence of the numerical parameters on the global response to be evaluated. The experimental displacement response, damage pattern, and OOP collapse mechanism are used as references. The study assesses: (i) different hourglass-control formulations; (ii) the evolution of artificial energy; (iii) damping techniques for high frequencies, such as Rayleigh coefficient β and linear bulk viscosity; (iv) linear elements with full and reduced integration and quadratic elements with full integration; and (v) computational time for implicit and explicit solvers. The results are intended to provide preliminary guidance for explicit FEM simulations of URM structures rather than definitive acceptance criteria. In this regard, the main contribution of this work is a preliminary assessment of potentially acceptable artificial-energy levels for three-dimensional URM models through comparison with experimental data. This requires a systematic evaluation of the user-defined parameters employed to control hourglass modes and limit the generation of artificial energy. A secondary objective is to evaluate the advantages and limitations of explicit solvers for simulating the nonlinear seismic response of URM structures by comparing their results and computational efficiency with those of widely used implicit solvers, which are generally considered reliable but can become computationally demanding when severe nonlinearities develop.

The paper is organised as follows. Section 2 describes the implicit and explicit time-integration procedures. Section 3 presents the numerical model and material properties. Section 4 discusses the energy balance and numerical artifacts associated with the element formulations. Section 5 defines the numerical parameters assessed. Section 6 presents the nonlinear dynamic analyses and discusses the numerical and experimental results. Finally, Section 7 summarises the main conclusions and limitations of the study.

2. Overview on Numerical Solvers for Nonlinear Dynamic Analysis

Direct time integration methods provide the numerical framework for obtaining the response of a structural system subjected to time-dependent loading (earthquakes, wind, blast, impact, etc.). These methods advance the solution incrementally by evaluating the equations of motion at successive time steps. They constitute one of the most advanced and computationally complex types of analysis for simulating the structural response of buildings. Within the framework of FEM modelling, the dynamic behaviour of a structural system with a nonlinear response can be described by the following equation:

$$\boldsymbol{M}\ddot{\boldsymbol{U}}(\mathrm{t}) + \boldsymbol{C}\dot{\boldsymbol{U}}(\mathrm{t}) + \boldsymbol{N}(\boldsymbol{U}(\mathrm{t})) = \boldsymbol{R}(\mathrm{t}) \tag{1}$$

where $\boldsymbol{M}$ is the mass matrix, $\boldsymbol{C}$ is the viscous damping matrix, $\boldsymbol{N}(\boldsymbol{U})$ is the vector of nonlinear internal forces, and $\boldsymbol{R}$(t) is the vector of time-dependent external forces. The vectors $\boldsymbol{U}$, $\dot{\boldsymbol{U}}$, and $\ddot{\boldsymbol{U}}$ represent displacement, velocity, and acceleration, respectively. The internal forces are related to the current displacement vector $\boldsymbol{U}$ at time t through a nonlinear function that can account for the constitutive material law, geometry, and boundary conditions. The transient problem consists of calculating the time-history solution for $\boldsymbol{U} = \boldsymbol{U}(t)$, starting from the initial conditions $\boldsymbol{U}(0) = \boldsymbol{U_o}$ and $\dot{\boldsymbol{U}}(0) = \dot{\boldsymbol{U}}_{\boldsymbol{o}}$, which are set to zero for ground motion.

In dynamic analysis, direct numerical integration methods divide the time into discrete intervals, Δt, and solve the equations of motion sequentially over these intervals, considering the variation in displacements, velocities, and accelerations at each time step. The complete response is therefore obtained through a sequence of problems in which the conditions are updated from one step to the next [6,32]. Different assumptions regarding the variations of $\boldsymbol{U}$, $\dot{\boldsymbol{U}}$, and $\ddot{\boldsymbol{U}}$ over each time interval lead to different integration schemes, which can be classified into implicit and explicit methods.

2.1. Implicit Solvers

In implicit solvers, the displacements at the current increment, $t + \Delta t$, are determined using the velocities and accelerations at the current step itself. Since these quantities are initially unknown, trial values are assumed and subsequently refined through an iterative procedure [6,32]. This procedure requires the solution of a system of equations involving the inversion of the stiffness matrix at each time step. Implicit methods are generally unconditionally stable, and the maximum time interval is therefore governed primarily by the required accuracy rather than by numerical stability [6]. Considerably larger time steps can be adopted than in explicit methods, reducing the total number of increments required for the analysis. Common implicit time integration schemes include the Houbolt, Wilson-θ, and Newmark methods [33]. The Newmark method is widely used for structural dynamic problems due to its accuracy and stability characteristics. In this formulation, the response at time $t+\Delta t$ is obtained by relating the velocities and displacements to the accelerations through [5]:

$$\dot{\boldsymbol{U}}_{t+\Delta t} = \dot{\boldsymbol{U}}_t + \Delta t\left[(1-\gamma)\ddot{\boldsymbol{U}}_t + \gamma\ddot{\boldsymbol{U}}_{t+\Delta t}\right] \tag{2}$$

$$\boldsymbol{U}_{t+\Delta t} = \boldsymbol{U}_t + \Delta t\dot{\boldsymbol{U}}_t + \Delta t^2\left[\left(\frac{1}{2}-\beta\right)\ddot{\boldsymbol{U}}_t + \beta\ddot{\boldsymbol{U}}_{t+\Delta t}\right] \tag{3}$$

where γ and β control the stability and numerical dissipation. Unconditional stability is attained when $\gamma \geq 0.05$ and $\beta \geq (2\gamma + 1)^2/16$. However, the numerical dissipation introduced by the Newmark method can also influence the response associated with the lower modes. The Hilber-Hughes-Taylor (HHT) method is an extension of the Newmark formulation that introduces the parameter α to provide numerical damping and allow larger time steps while maintaining stability. The method preserves the response at the lower frequencies, which are of primary interest in structural analysis, while damping the

spurious high-frequency modes [33]. This characteristic has led to the implementation of the HHT method in many FEM software packages. The parameter α is introduced into the Newmark formulation as [33]:

$$\gamma = \frac{1}{2} - \alpha,\ \beta = \frac{1}{4}(1-\alpha)^2, -\frac{1}{3} \leq \alpha \leq 0 \tag{4}$$

As α decreases, the numerical damping related to the high-frequency response increases.

If Equation (3) is solved for $\ddot{\boldsymbol{U}}_{t+\Delta t}$ in terms of $\boldsymbol{U}_{t+\Delta t}$ and then substituted in Equation (2), both solutions are given in terms of the unknown variable $\boldsymbol{U}_{t+\Delta t}$. Substituting these expressions in Equation (1) at time $t + \Delta t$ leads to a system of simultaneous equations. For nonlinear problems, the displacement increment vector, $\Delta\boldsymbol{U}$, needs to be solved; hence the equation of motion takes the form:

$$(a_0\boldsymbol{M} + a_1\boldsymbol{C} + \boldsymbol{K}_t)\Delta\boldsymbol{U} = \boldsymbol{R}_{t+\Delta t} + \boldsymbol{M}\left(a_2\dot{\boldsymbol{U}}_t + a_3\ddot{\boldsymbol{U}}_t\right) + \boldsymbol{C}\left(a_4\dot{\boldsymbol{U}}_t + a_5\ddot{\boldsymbol{U}}_t\right) - \boldsymbol{N}(\boldsymbol{U}_t) \tag{5}$$

where $\boldsymbol{K}_t$ is the stiffness matrix and the constants a_i are defined as:

$$a_0 = \frac{1}{\beta(\Delta t)^2};\ a_1 = \frac{\gamma}{\beta\Delta t};\ a_2 = \frac{1}{\beta\Delta t};\ a_3 = \frac{1}{\beta 2} - 1;\ a_4 = \frac{\gamma}{\beta} - 1;\ a_5 = \frac{\Delta t}{2}\left(\frac{\gamma}{\beta} - 2\right)$$

Since the internal force vector $\boldsymbol{N}(\boldsymbol{U}_t)$ is a nonlinear function of the displacement $\boldsymbol{U}$, governed by the constitutive material law and, when considered, geometrical nonlinearities and boundary conditions, the equilibrium solution cannot generally be obtained directly. Instead, iterative procedures, such as the regular, modified, or linear Newton-Raphson methods and the Quasi-Newton method, can be employed [3,5]. At each time increment, the iterations continue until the selected convergence criterion is satisfied, i.e., until the residual falls below a prescribed tolerance. Convergence can be evaluated in terms of forces, displacements, or energy.

2.2. Explicit Solvers

Explicit methods were originally developed for high-speed dynamic problems and are also suitable for structures exhibiting rapid stiffness degradation, including quasi-brittle materials such as masonry, for which convergence may be difficult to achieve using implicit schemes [6,34]. In an explicit formulation, the solution at time $t + \Delta t$ is determined from the equilibrium conditions at time t, using the values of $\boldsymbol{U}$, $\dot{\boldsymbol{U}}$, and $\ddot{\boldsymbol{U}}$ already known from the previous step. Therefore, the displacement vector at the end of the time increment does not depend on the loads or stiffness evaluated at the current time. This formulation facilitates the implementation of complex constitutive laws and avoids the inversion of the stiffness matrix, resulting in a low computational cost per time step [3,4].

However, explicit methods are conditionally stable and require small time increments to ensure numerical stability. The stable time increment is governed by the highest frequency of the discretised system or, equivalently, by the characteristic element dimension and the dilatational wave speed of the material [4,6,10]. The introduction of damping further reduces the stable time increment. Explicit integration schemes include the second-order central difference method, commonly adopted for large-scale stress analyses, and the fourth-order Runge–Kutta method. In the following, a brief overview of the central difference method is presented, as it is widely implemented in software packages.

The second-order central difference method assumes that, for a small time interval, the acceleration can be approximated from the velocities at the intermediate time steps [6,32]:

$$\dot{\boldsymbol{U}}_{t+\frac{1}{2}\Delta t} = \frac{\boldsymbol{U}_{t+\Delta t} - \boldsymbol{U}_t}{\Delta t} \tag{6}$$

$$\dot{\boldsymbol{U}}_{t-\frac{1}{2}\Delta t} = \frac{\boldsymbol{U}_t - \boldsymbol{U}_{t-\Delta t}}{\Delta t} \tag{7}$$

where $t - \Delta t$, t, and $t + \Delta t$ represent three successive times. The acceleration at time t is given by:

$$\ddot{\boldsymbol{U}}_t = \frac{\dot{\boldsymbol{U}}_{t+\frac{1}{2}\Delta t} - \dot{\boldsymbol{U}}_{t-\frac{1}{2}\Delta t}}{\Delta t} = \frac{1}{\Delta t^2}(\boldsymbol{U}_{t+\Delta t} - \boldsymbol{U}_t) - \frac{1}{\Delta t^2}(\boldsymbol{U}_t - \boldsymbol{U}_{t-\Delta t}) \tag{8}$$

Simplifying, it yields to:

$$\ddot{\boldsymbol{U}}_t = \frac{1}{(\Delta t)^2}(\boldsymbol{U}_{t+\Delta t} - 2\boldsymbol{U}_t + \boldsymbol{U}_{t-\Delta t}) \tag{9}$$

Substituting this expression into Equation (1) and rearranging leads to the solution of the nodal displacements:

$$\boldsymbol{U}_{t+\Delta t} = \Delta t^2 \boldsymbol{M}^{-1}\left(\boldsymbol{R}_t - \boldsymbol{C}\dot{\boldsymbol{U}}_t + \boldsymbol{N}(\boldsymbol{U}_t)\right) + 2\boldsymbol{U}_t - \boldsymbol{U}_{t-\Delta t} \tag{10}$$

Since the explicit software packages use a diagonal (lumped) mass matrix, the solution is trivial. The velocity at time $t + \Delta t$ is derived from the average velocities at times t and $t + \Delta t$ through:

$$\frac{1}{2}\left(\dot{\boldsymbol{U}}_t + \dot{\boldsymbol{U}}_{t+\Delta t}\right) = \frac{\boldsymbol{U}_{t+\Delta t} - \boldsymbol{U}_t}{\Delta t} \tag{11}$$

Rearranging, the previous equation takes the form:

$$\dot{\boldsymbol{U}}_{t+\Delta t} = \frac{2(\boldsymbol{U}_{t+\Delta t} - \boldsymbol{U}_t)}{\Delta t} - \dot{\boldsymbol{U}}_t \tag{12}$$

Once the displacements are calculated, changes in strain can be obtained along with the respective stress state according to the material constitutive law. Subsequently, the nodal internal forces $\boldsymbol{N}(\boldsymbol{U}_t)$ are computed, and the values for the equations are updated for the following time increment.

3. Numerical Modelling

The numerical model is based on a U-shaped specimen tested on the shake table at the University of Minho, Portugal. The specimen was assembled from hard granite blocks with dry joints. A stretcher bond was adopted, ensuring continuity between the orthogonal walls at the corners. At the base, the specimen was fully restrained, while the free ends of the sidewalls were vertically constrained by springs with a stiffness of 2147 kN/m. The springs were prestressed to apply a vertical force of 2.0 kN. Further details on the experimental setup and testing procedure are provided in [35], where a similar experimental campaign conducted on two comparable U-shaped specimens is described.

Masonry is a composite material that exhibits orthotropic behaviour due to the arrangement and mechanical interaction of its units and joints. Nevertheless, within a macro-modelling approach using FEM, masonry can be represented as an equivalent homogeneous continuum, an assumption widely adopted for the numerical analysis of large masonry structures. Under this approach, the selection of representative material properties and a suitable constitutive model is essential to reproduce the nonlinear response of unreinforced masonry.

The Concrete Damage Plasticity (CDP) model was adopted to describe the nonlinear behaviour of masonry. However, the representation of dry-joint masonry through a continuum macro-model presents particular challenges. The response of dry masonry is strongly governed by the interfaces between adjacent units, particularly by joint opening, closing,

sliding, and friction, which cannot be explicitly represented when the masonry assemblage is treated as an equivalent homogeneous continuum. This limitation is particularly relevant for the tensile response, since the tensile strength across dry joints is theoretically negligible. However, assigning a null tensile strength within the continuum constitutive model may lead to numerical difficulties. Therefore, a small non-zero tensile strength was adopted to approximate the low resistance to separation between masonry units while maintaining numerical stability. Consequently, some differences between the experimental and numerical responses are expected due to the inherent limitations of representing dry-joint masonry through a homogeneous continuum model.

3.1. Geometry and Mesh

The numerical model reproduces the actual geometry and dimensions of the tested specimen. It consists of a U-shaped masonry assemblage with a uniform wall thickness of 0.15 m, comprising two solid sidewalls and a front wall (façade) with an opening representing a doorway, as shown in Figure 1. The geometry was initially created in AutoCAD 2024 [36] and subsequently imported into Abaqus/CAE [37] for the generation of the numerical model. The experimental boundary conditions were also reproduced: the base of the model was fully restrained, while vertical restraint at the ends of the sidewalls was provided by two spring connector elements subjected to a prestressing force of 2.0 kN.

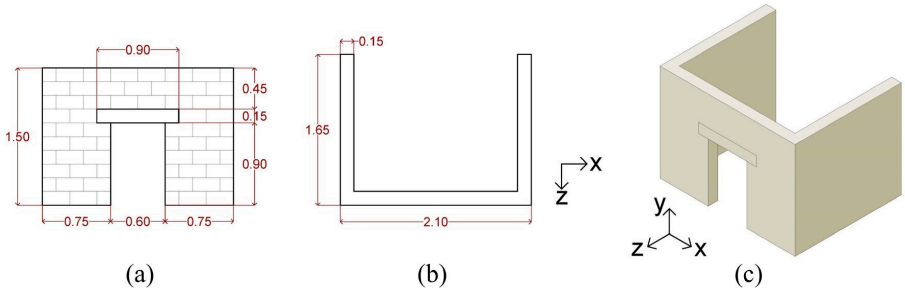


Figure 1. Geometry of the numerical model based on the tested specimen (dimensions in meters): (**a**) façade, (**b**) plan, and (**c**) isometric view.

According to the recommendations provided in the Abaqus User's Manual and Theory Manual [34,38], as well as previous numerical studies [39], at least four elements through the thickness are required to adequately reproduce bending behaviour. In this study, an average element size of 0.03 m was adopted, resulting in five elements through the 0.15 m wall thickness. The resulting mesh, shown in Figure 2, comprises 39,502 elements; the number of nodes depends on the element type (linear or quadratic). The influence of the element formulation on the numerical response is investigated and discussed later in this work.

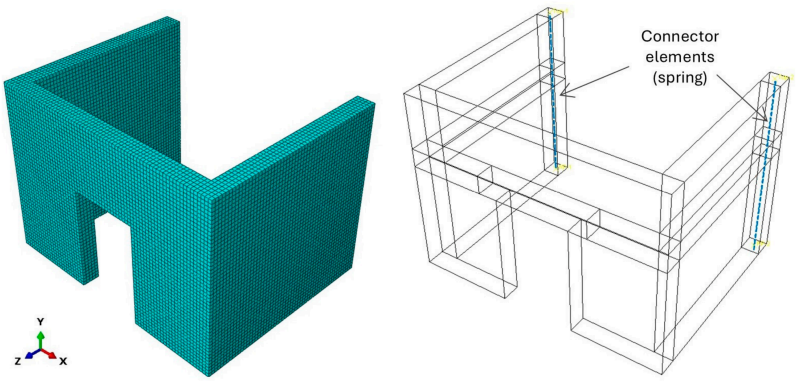


Figure 2. Mesh of the numerical model and location of the connector elements for the springs.

3.2. Material Properties

Dynamic identification tests were conducted to determine the natural frequencies and corresponding mode shapes of the specimen. These dynamic characteristics were subsequently used to calibrate the elastic properties of the numerical model. The calibration was performed through eigenvalue analysis by adjusting only the Young's modulus, since the mass, defined by a density of $\rho = 2580$ kg/m^3, and the boundary conditions were known.

Three vibration modes were considered for the calibration: one corresponding to the OOP response of the sidewalls, with an experimental frequency of 5.08 Hz, and two associated with the OOP response of the façade, with experimental frequencies of 8.30 Hz and 22.17 Hz. Although granite has a considerably high Young's modulus, approximately 74 GPa [35], the equivalent stiffness of the specimen is substantially lower due to the presence of dry joints between the masonry units. The calibration resulted in an equivalent Young's modulus of 155 MPa for the homogenised masonry. Figure 3 shows the three numerical mode shapes considered in the calibration, together with their corresponding frequencies. Mode 2 exhibited the largest difference with respect to the corresponding experimental frequency, with an error of approximately 12%. Modes 3 and 11, associated with the OOP response of the façade, are particularly relevant to the present study and showed good agreement with the experimental results, with differences in the corresponding frequencies of approximately 1.0%.

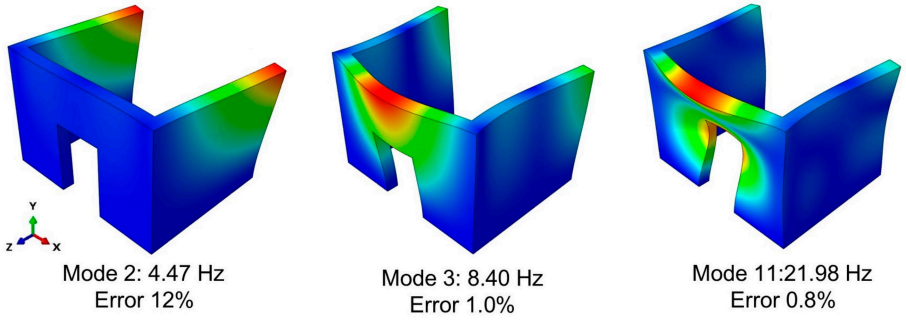


Figure 3. Numerical mode shapes and corresponding frequencies considered in the calibration.

The compressive strength of dry-jointed granite masonry, f_c, was obtained from the literature [40], where ten specimens composed of granite units with sawn contact surfaces were tested under compression. The compressive fracture energy, G_c, was estimated as a function of the compressive strength according to the following expression [3]:

$$G_c = \frac{32 f_c}{10 + f_c} \tag{13}$$

where the units are expressed in N/mm. Dry-jointed masonry has negligible tensile strength and, consequently, negligible tensile fracture energy. However, the CDP model requires non-zero values for these parameters to ensure numerical stability. Therefore, small values of tensile strength, f_t, and tensile fracture energy, G_t, were adopted to approximate the low resistance to separation between the dry-jointed masonry units while avoiding numerical issues. These values represent the homogenised behaviour of the units and dry joints within the walls. By contrast, the lintel consists of a single stone element, with the dry joints located only at its interfaces with the surrounding masonry. Higher tensile properties were therefore assigned locally to represent the monolithic character of the lintel. As expected for quasi-brittle masonry, the predicted cracking and collapse mechanisms were sensitive to the adopted tensile properties. Preliminary analyses were conducted using two limits for the mechanical properties of the lintel. Linear-elastic behaviour, considered an upper-bound case, prevented the formation of the central crack above the opening, whereas assigning the

homogenised wall tensile strength (f_t = 0.01 MPa), considered a lower-bound case, resulted in premature lintel failure. Therefore, an intermediate tensile strength of f_t = 0.02 MPa was adopted for the lintel. The absence of direct tensile measurements for the lintel remains a limitation of the model. Table 1 summarises the mechanical properties adopted to describe the nonlinear response of the masonry. The calibration and assessment stages were not fully independent, since the experimental frequencies and failure behaviour informed the selection of the material properties. However, once calibrated, these properties were kept unchanged in all subsequent analyses. The results should therefore be interpreted as a comparative assessment of the numerical formulations under a common material model rather than as an independent validation.

Table 1. Mechanical properties adopted for the numerical model.

	Density [kg/m^3]	**E [MPa]**	**Poisson's Ratio**	f_c **[MPa]**	f_t **[MPa]**	G_c **[N/mm]**	G_t **[N/mm]**
Walls	2580	155	0.2	73	0.01	28.14	0.025
Lintel	2580	155	0.2	73	0.02	28.14	0.025

Unreinforced masonry exhibits the typical nonlinear response of quasi-brittle materials, characterised by softening in tension and by hardening followed by softening in compression [41]. The CDP model is capable of representing these characteristics and is suitable for the simulation of quasi-brittle materials subjected to cyclic and dynamic loading [38]. Although initially formulated for concrete, the CDP model has also demonstrated its applicability to the nonlinear dynamic analysis of URM structures subjected to seismic actions [24,42–47]. This constitutive law assumes isotropic material behaviour and combines isotropic damaged elasticity with tensile and compressive plasticity. Its constitutive response is defined through the hardening/softening laws, damage evolution, yield criterion, and plastic flow rule. The uniaxial response is characterised independently in compression and tension. Stiffness degradation is represented through scalar damage variables $0 \leq d_c, d_t \leq 1$ for compression and tension, ranging from zero, corresponding to the undamaged state, to one, representing a complete loss of stiffness. To avoid numerical difficulties associated with a complete loss of stiffness, maximum damage values between 0.90 and 0.95 are commonly adopted. Within the CDP formulation, progressive degradation of the elastic stiffness initiates after the peak strength is reached [38]. In the absence of experimental data, the stiffness degradation was approximated following [34]:

$$d_c = 1 - \frac{\sigma_c}{f_c};\ d_t = 1 - \frac{\sigma_t}{f_t} \tag{14}$$

where σ_c and σ_t are the compressive and tensile stresses, respectively. Both damage variables were limited to a maximum value of 0.90.

The nonlinear compressive stress–strain relationship was defined using the mechanical properties listed in Table 1 and the formulation proposed by Feenstra [48]. Table 2 reports the compressive stresses and corresponding inelastic strains, ε_c^{in}, used to build the curve shown in Figure 4a, along with the associated scalar damage variable, d_c. Note that stiffness degradation initiates after the peak compressive strength is reached.

Table 2. Values for compressive response.

ε_c^{in}	σ_c(MPa)	d_c
0.00000	24.33	0.0000
0.01962	45.63	0.0000
0.07849	60.83	0.0000
0.17661	69.96	0.0000
0.31398	73.00	0.0000
0.63777	68.44	0.0625
1.02043	54.75	0.2500
1.46196	31.94	0.5625
1.91527	7.30	0.9000

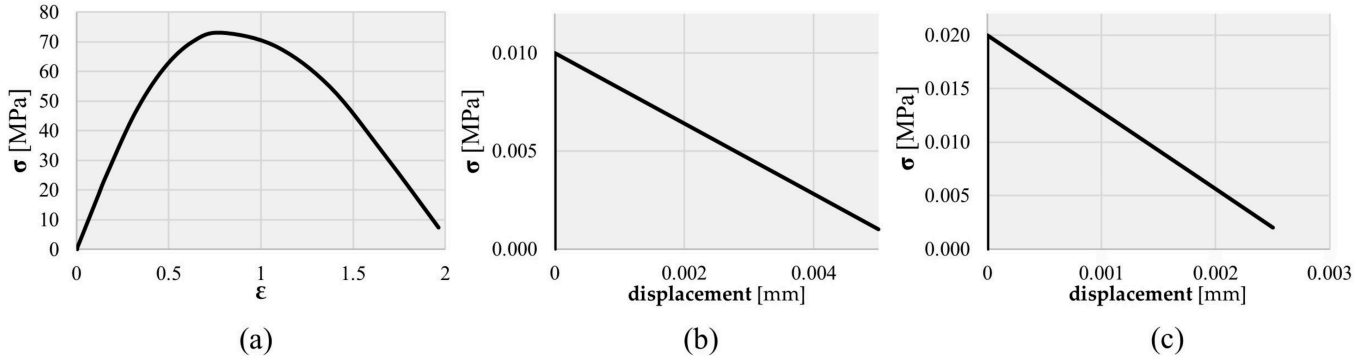


Figure 4. Nonlinear constitutive behaviour adopted for masonry: (**a**) uniaxial compressive stress–strain relationship; (**b**) tensile stress–displacement relationship for the walls; and (**c**) tensile stress–displacement relationship for the lintel.

In tension, a fracture-energy-based formulation was adopted to reduce the mesh dependency associated with strain-softening behaviour [49]. The tensile fracture energy controls the post-peak response. When the tensile fracture energy is specified directly, Abaqus defines the post-failure behaviour in terms of crack-opening displacement, u_{ck}, adopting a linear softening relationship expressed by [34]:

$$u_{ck} = \frac{2G_t}{f_t} \tag{15}$$

The resulting tensile stress–displacement relationships adopted for the walls and lintel are reported in Table 3 and illustrated in Figure 4b and Figure 4c, respectively. In addition, stiffness recovery associated with crack closure during the transition from tension to compression was considered in the dynamic analyses. Full recovery of compressive stiffness after cracking and no recovery of tensile stiffness after crushing were assumed by setting the weight factors to $w_c = 1$ and $w_t = 0$, respectively [38].

The yield criterion and plastic flow rule were defined using the parameters reported in Table 4. Although these parameters were originally formulated for concrete, similar values have been successfully adopted in numerical simulations of masonry structures [41,50].

Table 3. Values for tensile response.

Tension for Walls		
u_{ck} (mm)	σ_t (MPa)	d_t
0.00	0.010	0.00
0.01	0.001	0.90
Tensionfor Lintel		
0.00	0.020	0.00
0.00323	0.002	0.90

Table 4. Parameters adopted for the CDP yield surface and plastic flow rule.

Dilation Angle ψ	Eccentricity e	σ_{b0}/σ_{c0}	K
10°	0.1	1.16	2/3

4. Energy Balance and Numerical Artifacts

Energy quantities provide a useful means of evaluating the numerical quality of solutions obtained through explicit time integration [51]. From the conservation of energy principle, the total energy of the system, E_{total}, is expected to remain constant during the analysis. Considering that the structure is initially at rest, and therefore has no initial kinetic energy, the corresponding energy balance can be written as [38]:

$$E_I + E_V + E_K - E_W = E_{total} = 0 \tag{16}$$

where E_I denotes the internal energy, E_V accounts for the energy dissipated by the different damping mechanisms, including material damping, E_K represents the kinetic energy, and E_W is the work done by external forces. Numerical analysis satisfies energy conservation only approximately ($E_{total} \approx 0$), resulting in a small energy residual. The magnitude of this residual provides an indicator of the numerical accuracy of the solution and should remain below 1% ($E_{total}/E_W < 0.01$) throughout the simulation [51].

In structural analysis, different mechanisms contribute to the internal energy E_I:

$$E_I = E_E + E_P + E_{CD} + E_{DMD} + E_A \tag{17}$$

where the recoverable part corresponds to the elastic strain energy E_E, whereas energy is dissipated through plasticity E_P, viscoelasticity or creep E_{CD}, and damage E_{DMD}. An additional contribution, E_A, accounts for the artificial strain energy associated with the element formulation and its integration scheme.

Unlike the other contributions to the internal energy, artificial strain energy does not represent a physical (real) mechanism of the structural response. Instead, it is introduced by numerical procedures associated with the finite element formulation. Its interpretation therefore requires an understanding of the numerical artifacts that may develop depending on the selected element and the corresponding integration scheme.

Plane and hexahedral solid elements can be formulated using linear (first-order) or quadratic (second-order) shape functions, in combination with full or reduced integration schemes. Quadratic elements provide a higher-order interpolation of the displacement field and are generally more effective in representing curvature and bending behaviour. However, their higher number of nodes and integration points results in a considerably greater computational cost, even when reduced integration is employed. For large structural models, such as those representing historic buildings, this may become a significant limitation in nonlinear dynamic analyses, particularly when seismic assessment requires

a large number of simulations. Linear elements, in contrast, are computationally less demanding and may therefore offer an important advantage for large-scale models.

The 8-node linear hexahedral element is widely used in three-dimensional FEM analysis, particularly in explicit dynamics, metal forming, crashworthiness, and large-deformation solid mechanics. Its widespread use is mainly associated with its computational efficiency, robustness, and suitability for discretising large volumes, and generally better convergence properties than tetrahedra elements [52]. However, depending on the integration scheme, linear hexahedral elements may be affected by two well-known numerical artifacts: shear locking and hourglass (zero-energy) modes, as illustrated in Figure 5. Both phenomena can significantly compromise the accuracy of the numerical response, particularly in bending-dominated problems [28–30].

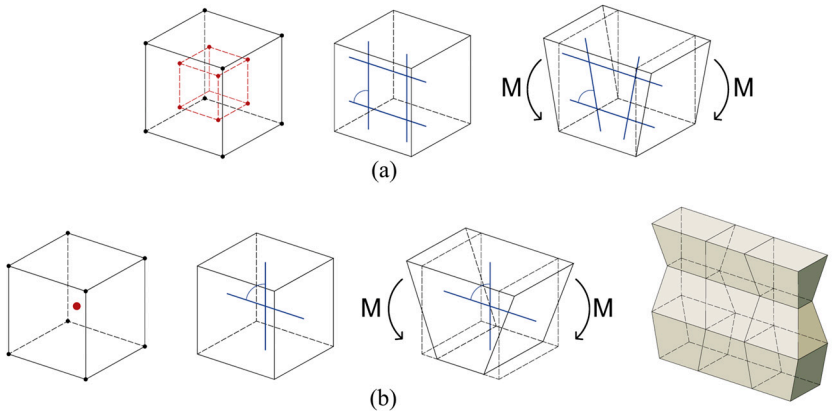


Figure 5. Numerical artifacts associated with linear hexahedral elements: (**a**) shear locking under bending deformation, showing the integration scheme and deformation field; and (**b**) hourglass (zero-energy) mode, showing the integration scheme, deformation field, and propagation through the mesh.

The conventional 8-node fully integrated element uses eight integration points, as illustrated in Figure 5a (red dots). Shear locking may occur in this element type when subjected to bending. Due to the linear interpolation of the displacement field, the element cannot reproduce curvatures without introducing spurious shear strains at the integration points. Consequently, the element develops an artificially high flexural stiffness, leading to an underestimation of displacements [28]. Shear locking is more likely to develop in coarse or irregular meshes, where poorly shaped elements can introduce additional spurious strain components [28]. Mesh refinement and the use of regular elements can mitigate shear locking, although the phenomenon cannot be completely eliminated [53]. The adoption of reduced (one-point) integration elements addresses this limitation but may introduce hourglass deformation modes (Figure 5b).

Hourglass modes, also referred to as zero-energy modes, are deformation patterns that generate no strain energy at the element level [54–56]. In reduced-integration elements, the use of fewer integration points results in an incomplete evaluation of the stiffness matrix, such that certain deformation patterns have no associated stiffness. For an 8-node hexahedral element, specific nodal displacements can occur while the neutral axes passing through the integration point remain unchanged in length and rotation [3] (Figure 5b). Consequently, the deformation produces no strain variation at the integration point and, therefore, no corresponding stress or internal resisting force. The nodes are thus free to deform without the appropriate energetic contribution. Hourglass modes may be triggered by bending, concentrated loads, or boundary conditions, particularly in coarse or irregular meshes. If insufficiently controlled, these spurious deformation patterns can propagate through the mesh, as illustrated in Figure 5b, and eventually leading to

meaningless solutions [54]. Mesh refinement and regular discretisation can reduce their development and propagation; for bending-dominated problems, at least four elements through the thickness are recommended [34]. In addition, several numerical techniques have been developed to suppress hourglass modes by introducing artificial forces against the corresponding deformation patterns.

The artificial resisting forces used to control hourglass modes are reflected in the artificial strain energy, which may progressively accumulate during the analysis and eventually reach levels comparable to the physical energy components [57]. Excessive artificial strain energy may therefore introduce significant errors and compromise the reliability of the numerical response. The performance of different hourglass control techniques, particularly regarding the generation of artificial strain energy during nonlinear dynamic analyses of URM, is evaluated later in this study.

It should be emphasised that shear locking and hourglass modes are not intrinsic to the explicit time integration method. They arise from the spatial formulation and numerical integration of the finite elements and may therefore occur in analyses performed using either explicit or implicit solution procedures.

5. Numerical Modelling Parameters Assessed for Nonlinear Dynamic Analysis

5.1. Parameter 1: Hourglass Control

To mitigate the development of hourglass modes, numerical solvers commonly introduce artificial stiffness or viscous (damping) forces [58]. Abaqus provides several hourglass control formulations intended to suppress their initiation and propagation [34]. The available formulations include the relax stiffness, Kelvin viscoelastic, and enhanced approaches. The relax stiffness method employs a relaxation function to control the evolution of hourglass deformation over time by introducing numerical damping that dissipates energy associated with these spurious modes, particularly under high-frequency response or sharp deformation gradients. The method is particularly suitable for problems involving sudden dynamic loading. The magnitude of the hourglass control can be modified through a scale factor, s, which regulates the amount of artificial resistance introduced into the numerical solution.

The Kelvin viscoelastic approach combines elastic and viscous contributions to generate the artificial forces. The formulation is expressed as:

$$Q = s\left[(1-a)Kq + aC\frac{dq}{dt}\right] \tag{18}$$

where Q is the artificial force, q represents a displacement of the hourglass mode, K and C are the stiffness and viscous coefficient, respectively, and a is a weight factor that determines the relative contribution of the stiffness and viscous components. Depending on the value of a, the formulation can represent pure stiffness control ($a = 0$), pure viscous control ($a = 1$), or a combination of both ($0 < a < 1$). The stiffness component generates a restoring force related to the nodal displacements, thereby providing resistance against hourglass deformation. If the introduced stiffness remains sufficiently small, its influence on the physical response is limited [54]. The viscous component generates an artificial force proportional to the nodal velocity. This contribution dissipates energy and delays the development of hourglass deformation but does not provide a restoring force and therefore cannot stabilise the mode [54]. Moreover, the viscous contribution may reduce the stable time increment in explicit integration. The magnitude of the artificial forces can be adjusted through the scale factor, s. The default values in Abaqus for the explicit solver correspond

to pure stiffness control (a = 0) with scale factor s = 1.0. Further details of the formulation are provided in [54].

The selection of the hourglass control formulation and the corresponding scale factor depend on the characteristics of the problem, since material properties, geometry, load distribution, and other factors influence the onset and propagation of hourglass modes. For material models involving plasticity, such as CDP, the hourglass stiffness should be scaled down to avoid an excessively stiff element response [52,59].

The enhanced method is a refinement of the pure stiffness formulation (Equation (18) with a = 0) developed to provide greater resistance to hourglass modes in nonlinear materials. Although this approach is generally effective, it may result in an excessively stiff response in problems involving plastic yielding under bending [59]. The formulation introduces stabilising forces determined from the element geometry and material properties without requiring user-defined parameters; therefore, the scale factor, s, is not applicable. Further details of the formulation are provided in [52,59]. Table 5 summarises the hourglass control methods investigated in this study, together with the adopted values of the scale factor, s, when applicable, and the weight factor, a.

Table 5. Hourglass control methods adopted in the analyses and corresponding weight and scale factors for elements with reduced integration.

Hourglass Control	Weight Factor a	Scale Factor s			
Default [1]	0.00	1.0			
Enhanced	N/A	N/A			
Relax stiffness	N/A	0.01	0.03	0.05	0.10
Stiffness (pure)	0.00	0.01	0.03	0.05	0.10
Combined	0.25	0.01	0.03	0.05	0.10
Combined	0.50	0.01	0.03	0.05	0.10
Combined	0.75	0.01	0.03	0.05	0.10

[1] Default hourglass control in Abaqus for explicit analysis.

Since hourglass control introduces artificial energy into the numerical solution, its magnitude can be used as an indicator of the reliability of the analysis. According to [34,51], the artificial energy should remain below 1.0% of the internal energy. However, this criterion appears to be more appropriate for quasi-static analyses, where the loading rate is relatively low, and may be restrictive for dynamic analyses involving faster deformations. Higher limits have been considered in previous studies. Belytschko et al. [59] suggested that artificial energy levels of 5.0% or higher indicate significant spurious deformation when the enhanced hourglass control is employed. Zheng et al. [58] adopted a limit of 5.0% in the numerical analysis of a lunar lander during landing, whereas Storheim et al. [31] considered a tolerance of up to 10.0% when simulating metal deformation due to collision. In all three studies, the material behaviour was represented using elastic-plastic constitutive models, which may influence the generation of artificial energy [59]. However, reference limits for artificial energy in the nonlinear dynamic analysis of URM and other quasi-brittle materials are currently lacking. Therefore, one of the objectives of the present study is to provide insight into acceptable levels of artificial energy for the nonlinear dynamic analysis of URM buildings using the CDP model, as well as to evaluate suitable hourglass control methods and parameters. Nevertheless, further investigations involving additional models validated against experimental results are required to establish more robust criteria.

5.2. Parameter 2: Rayleigh Damping in the Explicit Method

For an explicit time integration scheme, numerical stability depends on the highest frequency of the structural system. The size of the time increment is therefore restricted by a critical value associated with the maximum angular frequency, ω_{max}. For an undamped system, the stability condition can be written as [60]:

$$\Delta t \leq \Delta t_{cr} = \frac{2}{\omega_{max}} \tag{19}$$

where Δt_{cr} is the critical time increment. Accordingly, the time step used in the analysis must remain below this limit to ensure a stable numerical solution. The introduction of damping modifies this stability condition and reduces the time increment. For a damped system, the critical time increment can be expressed as a function of the damping ratio associated with the highest frequency of the model:

$$\Delta t \leq \Delta t_{cr} = \frac{2}{\omega_{max}} \left(\sqrt{1 + \xi_{max}^2} - \xi_{max} \right) \tag{20}$$

where ξ_{max} is the damping ratio corresponding to ω_{max}. In explicit analyses, damping is commonly introduced through Rayleigh damping in commercial software packages [34]. This formulation relates the damping matrix, $\boldsymbol{C}$, to the mass matrix, $\boldsymbol{M}$, and the stiffness matrix, $\boldsymbol{K}$ through [61]:

$$\boldsymbol{C} = \alpha \boldsymbol{M} + \beta \boldsymbol{K} \tag{21}$$

where α is the mass-proportional damping coefficient, which controls the low-frequency range, whereas β is the stiffness-proportional damping coefficient and governs the high frequencies. For a given angular frequency, ω_a, the corresponding damping ratio is obtained from:

$$\xi = \frac{\alpha}{2\omega_a} + \frac{\beta \omega_a}{2} \tag{22}$$

The coefficients α and β are generally selected over a frequency interval that contains the vibration modes relevant to the dynamic response [62]. If the maximum frequency of interest is high ($\omega_a = \omega_{max}$), the mass-proportional contribution becomes negligible in the evaluation of the stability limit (Equation (20)), whereas the stiffness-proportional damping considerably reduces the time increment. For large models, this reduction can result in a substantial increase in computational cost and may render the analysis impractical. For this reason, stiffness-proportional damping is frequently omitted in explicit analyses by setting $\beta = 0$, while damping is introduced only through the coefficient α [63,64]. This assumption considers that the structural response is primarily driven by the lower frequencies and, consequently, by the mass contribution [6]. If stiffness-proportional damping is included, it is recommended that the value of β be of the same order of magnitude as, or smaller than, the stable time increment of the undamped system to limit its influence on the time increment [34].

A damping ratio of 3% was adopted for the numerical model [65–67]. The Rayleigh damping coefficients were determined considering the first frequency obtained from the eigenvalue analysis, 4.28 Hz (26.87 rad/s), and the highest frequency of interest, corresponding to Mode 11, 21.98 Hz (138.11 rad/s). The modes within this frequency range account for approximately 70% of the cumulative modal mass participation. By solving Equation (22), the resulting coefficients were $\alpha = 1.34957\ s^{-1}$ and $\beta = 0.000364$ s. Three conditions were then considered for the stiffness-proportional damping coefficient: $\beta = 0$, the value obtained from Equation (22), and 10% of this value. The comparison allows the

influence of stiffness-proportional damping on the structural response and the stable time increment to be evaluated.

5.3. Parameter 3: Linear Bulk Viscosity

In Abaqus, linear bulk viscosity, also known as truncation frequency damping, provides an additional source of damping in the numerical solution but does not form part of the material constitutive law [34]. It acts through the volumetric strain rate and is primarily intended to suppress numerical oscillations associated with the highest frequencies of the model. Bulk viscosity pressure, p, is defined as a linear function of the volumetric strain rate, $\dot{\varepsilon}_{vol}$, as:

$$p = b\rho c_d L^e \dot{\varepsilon}_{vol} \tag{23}$$

where b is a damping coefficient, ρ is the current material density, c_d is the current dilatational wave speed, and L^e is the characteristic element length. Since linear bulk viscosity primarily introduces damping at high frequencies, its effect on the numerical response may be comparable to that produced by the stiffness-proportional coefficient β in the Rayleigh damping formulation. Therefore, its influence on both the structural response and the stable time increment was investigated. Five values for b were considered based on a previous study [25]: 0.01, 0.06 (default value), 0.50, 1.00, and 5.00.

Although Rayleigh damping and linear bulk viscosity attenuate high-frequency components of the response, they have different purposes. Rayleigh damping was adopted to represent physical energy dissipation at the structural level by assigning target damping ratios to a range of vibration modes. Linear bulk viscosity, in contrast, is a numerical damping technique used to reduce high-frequency oscillations through the volumetric strain rate and does not represent physical material or structural damping.

5.4. Parameter 4: Element Type

Finally, the behaviour of the model was investigated considering different element types and time integration methods (implicit and explicit solvers). In addition to the direct comparison of the structural responses, the computational time and storage requirements associated with the generated data were evaluated. For the implicit method, three element types were assessed: linear with full integration, linear with reduced integration, and quadratic with full integration. For the explicit method, the linear element with full integration was also considered, in addition to the set of analyses presented in Table 5. Abaqus provides only linear elements for the explicit solver; thus, quadratic elements were not evaluated. The implicit solver in Abaqus is based on the HHT method and uses the Newton-Raphson method to solve nonlinear problems. The implicit analyses in this work employed the full Newton solution technique without modifying its default settings, together with the HHT integration scheme with the default parameters $\alpha_{\mathrm{HHT}} = -0.05$ corresponding to $\gamma_{\mathrm{HHT}} = 0.55$ and $\beta_{\mathrm{HHT}} = 0.275625$. Since geometric nonlinearities are inherently accounted for in the explicit formulation, they were also included in the analyses performed with the implicit solver to ensure a consistent comparison between both integration methods.

6. Nonlinear Dynamic Analysis

6.1. Seismic Signal

Previous experimental and numerical investigations have demonstrated that near-fault ground motions can trigger the OOP collapse of URM walls [68–71]. In the experimental campaign, two records with different characteristics, classified as moderately pulse-like and non-pulse-like, were selected from the European Strong Motion Database (ESM) [72]. Further details on the selection criteria are provided in [35,73]. For the present numerical study, only the non-pulse-like record EMSC−20160824_0000006 was considered. The record

corresponds to the 2016 Amatrice earthquake in Italy (M_w 6.0) and was recorded at the Norcia station, with an original PGA of 0.236 g. Prior to the experimental tests, the signal was calibrated according to the characteristics of the shake table [35]. The signal shown in Figure 6 corresponds to the motion recorded on the shake table and was therefore adopted as the reference input for the numerical analyses.

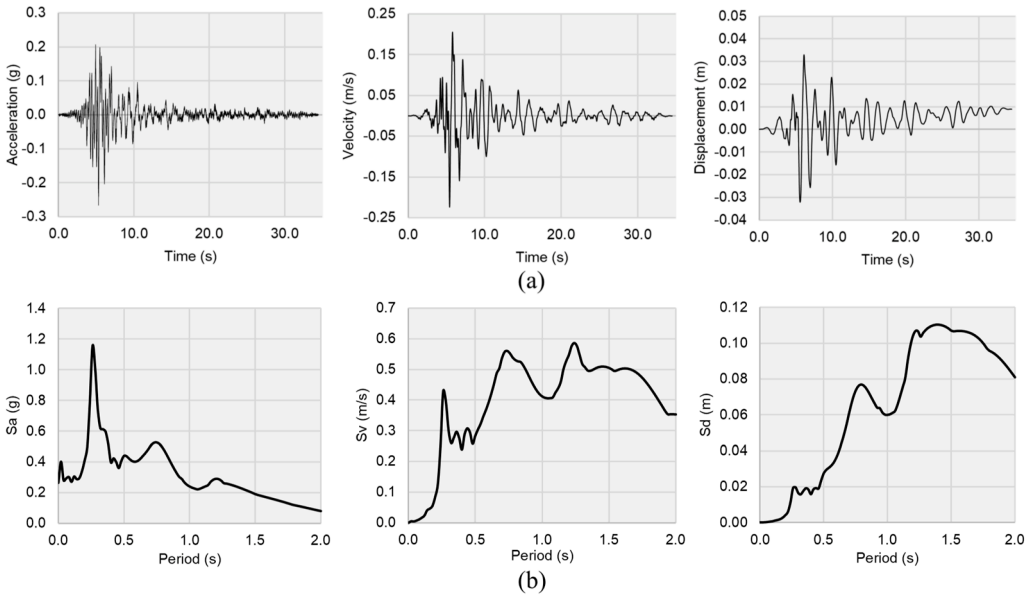


Figure 6. Selected input signal: (**a**) acceleration, velocity, and displacement time histories, (**b**) spectral accelerations, velocities, and displacements.

The non-pulse-like signal was selected for this study because its cyclic characteristics allow the specimen to undergo several loading reversals before collapse. This provides a suitable loading condition for evaluating the progressive development of artificial strain energy and its influence on the numerical response. During the experimental campaign, the ground motion was applied incrementally, and the first OOP collapse of the façade occurred at a PGA of 0.410 g. It should be noted that the specimen was restored after each test by rebuilding the deformed portions, polishing the contact interfaces, and replacing damaged blocks. Therefore, the test at 0.410 g was performed on an undamaged specimen, without accumulated damage from the preceding lower-intensity tests. Accordingly, the reference signal was scaled to the same PGA for the numerical analyses, allowing the response and artificial energy generation to be evaluated up to the experimentally observed collapse level. The seismic input was applied as a prescribed velocity history, as this form of boundary condition is particularly suitable for the central difference integration scheme employed by the explicit solver [34].

The analyses consisted of two steps. In Step 1, the self-weight of the model was applied using a smooth loading function over a duration of 1.0 s. Since gravitational loading should be applied under quasi-static conditions, the selected duration and loading function were intended to minimise the generation of inertial forces during this step. Step 2 consisted of applying the velocity time-history at the base of the model. As previously mentioned, the record corresponding to the experimental test in which the mock-up collapsed was considered in this study. Collapse occurred at 6.62 s; therefore, the first 8.0 s of the velocity time-history were considered in the numerical analyses. For the implicit analyses, the initial time increment was set to 0.002 s, corresponding to approximately 1/20 of the period of Mode 11 (0.046 s), the highest vibration mode of interest, and satisfying the condition for the accuracy criterion according to [61]. Automatic time incrementation was also enabled for the implicit analyses, with the minimum allowable time increment set to 1.0×10^{-5} s.

For the explicit analyses, Abaqus automatically calculated and updated the stable time increment throughout the simulation.

6.2. Results

All analyses were performed using Abaqus/CAE 2025 [37] on the same computer, equipped with a 16-core AMD Ryzen 9 9950X processor operating at 4.3 GHz and 192 GB of RAM. Each job was executed using four CPU cores under the same parallel-processing configuration. It should be noted that the explicit analyses were performed using double precision. For the implicit analyses, the default strict convergence criteria were retained, corresponding to a force-residual tolerance of 0.5% and a displacement-correction tolerance of 1%.

The comparison between the experimental and numerical results was primarily performed in terms of the displacement time-history at the centre of the façade, where the largest deformation developed during the experimental double-bending mechanism. Although displacement histories at several locations would provide a more complete quantitative description of the façade deformation, only the central displacement history was available for the present study. The damage patterns were therefore assessed qualitatively, as quantitative experimental measurements of crack location, damaged area, and individual block rotation were not available. Given the homogenised continuum modelling approach, exact agreement between the experimental and numerical damage patterns was not expected. Accordingly, the validation focused on the global displacement response and collapse mechanism rather than the detailed local behaviour of individual masonry units.

In the first stage, a series of nonlinear dynamic analyses was conducted using the explicit solver to evaluate the influence of the different hourglass-control formulations listed in Table 5 on the response and the generation of artificial energy (Parameter 1, Section 5.1). Figure 7 presents the displacement time histories and compares them with the experimental response. The experimental displacement history could be reliably tracked up to approximately 300 mm. At this displacement, large rotations caused the central masonry blocks to lose stability and subsequently fall, after which their speckle patterns were no longer visible to the DIC cameras. Physical collapse was consistently observed once this displacement was reached during the experimental campaign. Moreover, 300 mm corresponds to twice the wall thickness and therefore represents a very large out-of-plane displacement. The numerical histories were truncated at the same value to ensure consistency with the available experimental measurements. Thus, the 300 mm value was based on the observed physical collapse and the measurement limit of the DIC system rather than on an arbitrary numerical threshold.

All models reproduced the experimental response reasonably well up to approximately 4.0 s, when damage began to develop in the numerical models. The responses started to diverge before 6.0 s as nonlinear behaviour became predominant. A clear trend was observed when the artificial forces were defined as a function of the nodal displacements: the numerical response became progressively stiffer as the scale factor s increased, delaying the collapse. By contrast, the formulations incorporating predominantly velocity-dependent artificial forces (Combined with a = 0.75) produced similar responses. Both the default formulation (stiffness control with a = 0 and s = 1.0) and the enhanced hourglass-control formulations underestimated the displacement response.

One of the main concerns associated with linear elements with reduced integration is the generation of artificial energy. Limits between 5% and 10% of the internal energy have been proposed by [31,58] for analyses involving metallic materials. However, their applicability to nonlinear dynamic analyses of URM structures, particularly when extensive damage or collapse occurs, has not been established. However, their applicability to

nonlinear dynamic analyses of URM structures, particularly when extensive damage or collapse occurs, is unclear. To the authors' knowledge, suitable limits have not been systematically investigated for this type of analysis. Thus, the present study provides a preliminary assessment of whether these values may serve as reference limits for evaluating artificial energy in nonlinear dynamic simulations of URM structures, although further research is needed to assess their broader applicability and define more robust criteria.

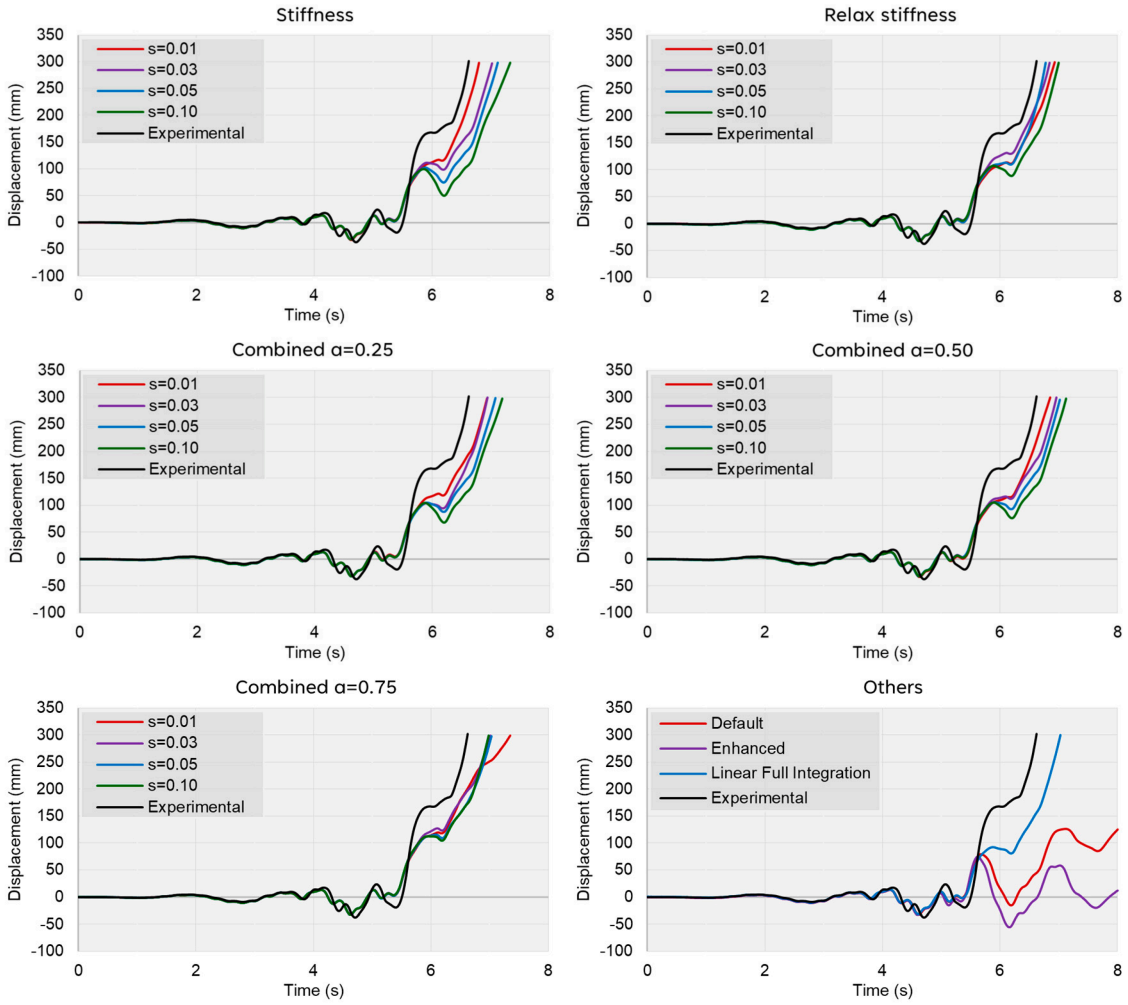


Figure 7. Experimental and numerical results in terms of displacements, using different hourglass-control formulations and different scale factors, *s*.

Figure 8 presents the evolution of the artificial energy generated by each hourglass-control formulation and value for the scale factor *s*, expressed as the ratio E_A/E_I. Each time history was truncated when the corresponding analysis reached a displacement of 300 mm. During the predominantly elastic phase, up to approximately 4.0 s, this ratio remained stable. For the stiffness formulations, in which the artificial forces depend on nodal displacements, the ratio remained below 1%. By contrast, for the combined formulations incorporating velocity-dependent forces, it reached approximately 3.5% during this initial phase.

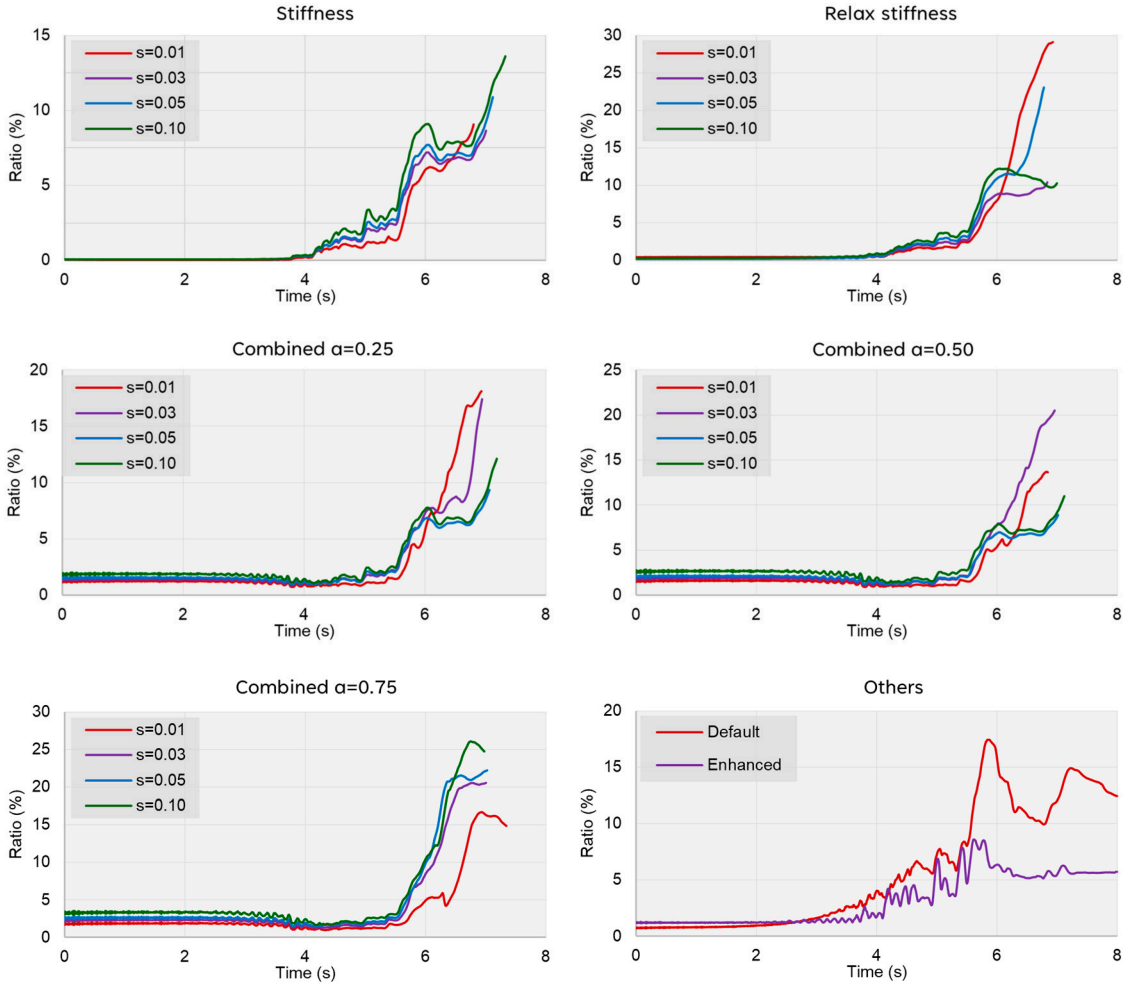


Figure 8. Artificial energy generated by different hourglass-control formulations and different *s*.

As the ground-motion amplitude increased, element deformation and material damage also increased. The stiffness degradation represented by the CDP model resulted in more flexible and increasingly distorted elements, requiring a greater contribution from the artificial forces to suppress spurious deformation modes. Unlike the displacement response, the artificial energy ratio did not exhibit a clear relationship with the selected scale factor. However, during damage propagation, the ratio remained at approximately 5–7% in most analyses, while some models reached the collapse displacement before the ratio exceeded 10%.

Figure 9 compares the experimental and numerical damage patterns at the instant when the displacement at the centre of the façade reached 300 mm. Experimentally, collapse was governed by OOP double bending of the façade. The upper masonry units at the corners rotated, producing diagonal cracks inclined at approximately 45° in the sidewalls. The collapse mechanism involved the portion of the façade above the door opening. Figure 9 presents the tensile damage patterns obtained from a representative model of each hourglass-control family (stiffness, relax stiffness, and combined). The models were selected by considering their agreement with the experimental collapse time and the amount of artificial energy generated. All three selected models captured the global OOP collapse mechanism of the façade, although the local experimental damage features were only partially reproduced. Nevertheless, differences were observed in the damage patterns. The numerical models did not reproduce either the rotation of the upper corner units or the approximately 45° cracks in the sidewalls. The three models exhibited tensile

damage at the midspan of the façade above the door opening, together with bending cracks near the base. Some variations were also observed among the damage patterns among the models. The type of hourglass-control formulation influences the damage distribution and extension, although their global responses remained consistent.

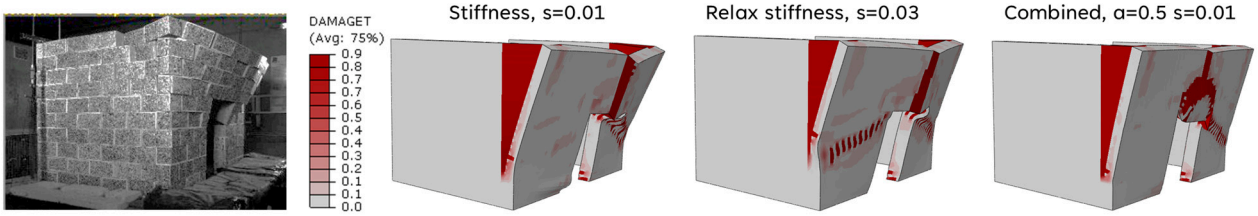


Figure 9. Deformation and damage immediately before experimental collapse, compared with the deformation and tensile damage distributions predicted by three numerical models at a displacement of 300 mm (collapse).

The subsequent phase evaluated the influence of two techniques for damping of high frequencies on the dynamic response, artificial energy generation, and the stable time increment: the introduction of the damping parameter β and the application of linear bulk viscosity, defined by b. For this purpose, only the three models previously selected from the respective hourglass-control families were considered: Stiffness with $s = 0.01$, Relax stiffness with $s = 0.03$, and Combined with $a = 0.5$, $s = 0.01$. As described in Sections 5.2 and 5.3, two values of β were adopted: the calculated value of $\beta = 0.000364$ s (models denoted by β) and a reduced value of 3.64×10^{-5} s (models denoted by 0.1 β). The reduced value was of the same order of magnitude as the stable time increment obtained for the models without damping, as recommended by [34]. For the linear bulk viscosity parameter b, values of 0.01, 0.06 (the default value), 0.50, 1.0, and 5.0 were considered.

Figure 10 compares the numerical displacement time histories with the experimental results. The models incorporating the damping coefficient β were unable to reproduce the experimentally observed collapse. When the full value of β was adopted, the response remained predominantly in the elastic range, with negligible damage. Regardless of the hourglass-control formulation, the three models exhibited the same response in terms of displacements. The models with the reduced value of β exhibited some permanent deformation and moderate damage, although they still failed to reproduce the collapse. A similar response was obtained when the bulk viscosity was set to 5.0. By contrast, values between 0.01 and 1.0 delayed the onset of collapse in most of the analyses.

Figure 11 shows the evolution of artificial energy for these analyses. In most models that did not predict collapse, the artificial energy ratio remained below 5%. This result was expected because damping of the numerical high-frequency response limited the development of damage and large deformations. The results suggest that 5% may be considered a preliminary reference limit for dynamic analyses in which the response remains predominantly elastic. Nevertheless, among models that reproduce the structural response adequately, formulations and parameters that generate lower levels of artificial energy should be preferred.

The models that predicted collapse exhibited different levels of artificial energy. Some reached the collapse displacement before the artificial energy ratio exceeded 10%, particularly those employing stiffness-based hourglass control, for which the artificial forces are proportional to the nodal displacements (see the Stiffness and Relax Stiffness results in Figure 11). Together with the analyses performed without the damping coefficient β and bulk viscosity, these results suggest that large displacements and collapse in masonry can be reproduced while maintaining the artificial energy ratio at approximately 10% or

below. However, this value should be regarded as a preliminary reference rather than a definitive limit.

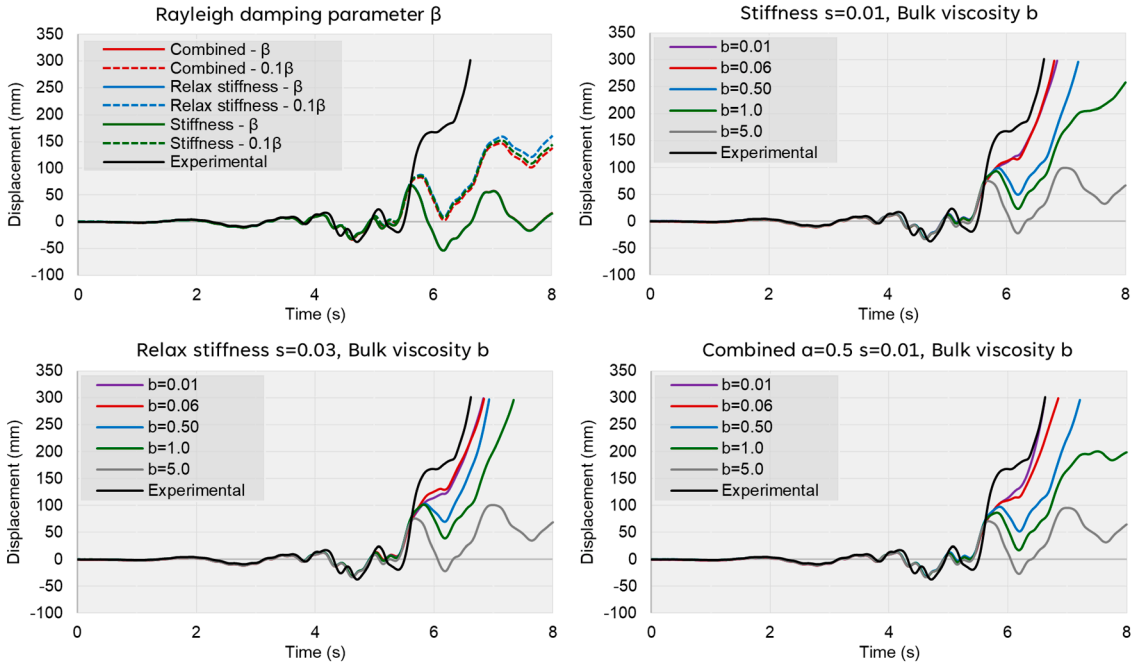


Figure 10. Experimental and numerical results in terms of displacements for three different hourglass-control formulations, using the damping parameter β and bulk viscosity b.

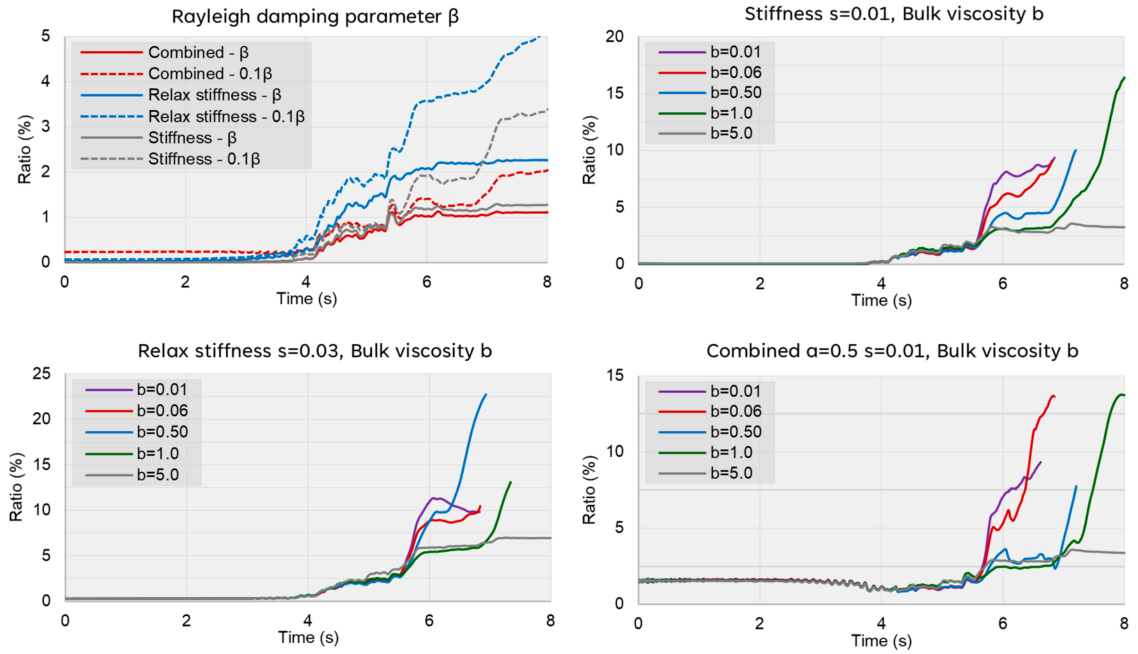


Figure 11. Artificial energy generated by different hourglass-control formulations using the damping parameter β and bulk viscosity b.

The initial stable time increments of the explicit analyses are summarised in Figure 12. The largest increments, between 7.0×10^{-5} and 8.0×10^{-5} s, corresponded to the models incorporating only mass-proportional damping coefficient α. When the full calculated value of the stiffness-proportional coefficient β or b = 5.0 was adopted, the stable time increment decreased by approximately a factor of seven. Therefore, these values increased the com-

putational demand without improving the numerical prediction, since the corresponding models did not reproduce collapse.

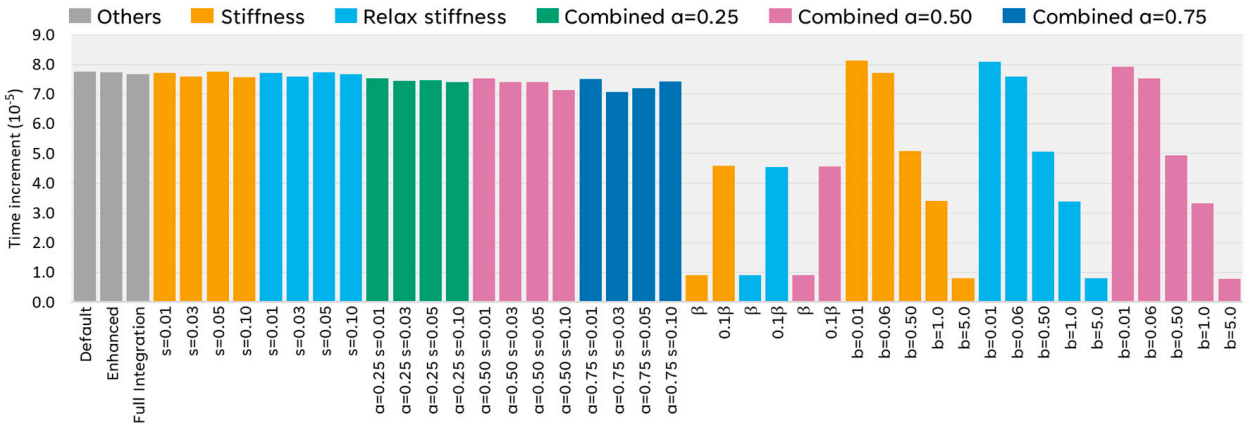


Figure 12. Stable time increment for different hourglass-control formulations, scale factor s, damping parameter β, and bulk viscosity b.

In the final stage, nonlinear dynamic analyses were performed using the implicit solver to compare the two time-integration procedures and assess the influence of the element formulation on the numerical response, computational time, and output-file size. Three element formulations were considered: linear elements with full integration, linear elements with reduced integration using the Stiffness hourglass-control (s = 0.01), and quadratic elements with full integration. Figure 13 compares the displacement time histories obtained using the implicit solver with those obtained using the explicit solver for models incorporating the full value of the damping coefficient β. All three implicit models produced displacement responses similar to those obtained with the explicit solver, underestimating the experimental displacements and deformations. Negligible damage developed throughout the analyses, and the models remained predominantly within the elastic range. These results demonstrate that, for this case study, the damping coefficient β strongly influences the dynamic response regardless of the time-integration method adopted. Thus, the implicit and explicit solvers produced similar results within the elastic range.

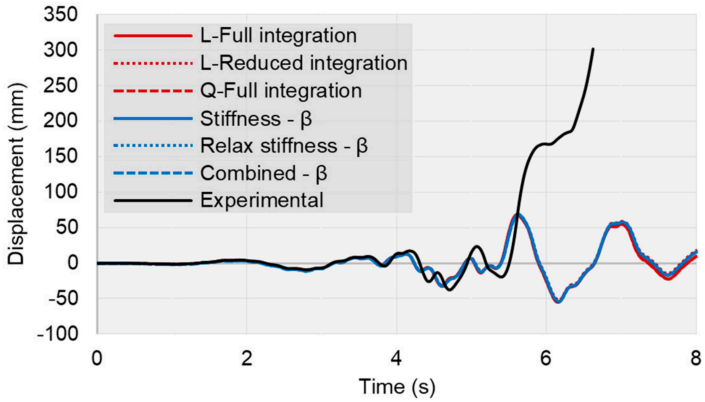


Figure 13. Response comparison between the implicit and explicit solvers. Abbreviations indicate: L (linear element) and Q (quadratic element).

Figure 14 summarises the computational time, expressed in hours and minutes, required for each analysis using the implicit and explicit solvers. Overall, the explicit solver completed the dynamic analyses faster than the implicit solver. However, the difference between the two solvers was relatively small for the models incorporating the full value of β and for those using bulk viscosity (b = 5.0).

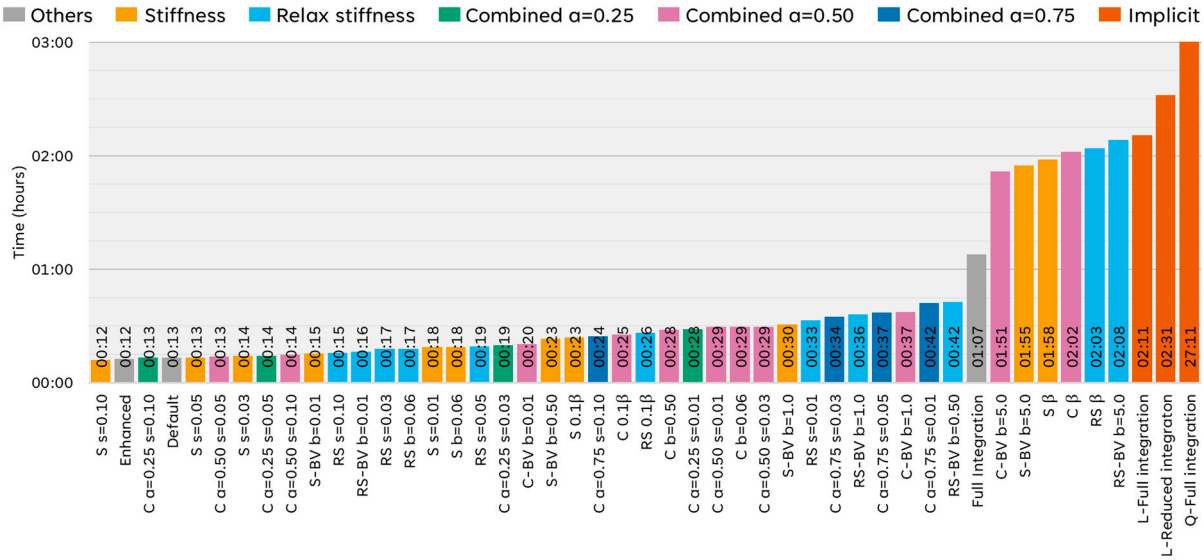


Figure 14. Computational time for the explicit and implicit analyses according to element type, hourglass-control formulation, and damping technique. Values within the bars indicate the computational time in hours and minutes (hh:mm). Abbreviations: S, stiffness; RS, relax stiffness; C, combined; BV, bulk viscosity; L, linear element; and Q, quadratic element.

Regarding output-file size, all analyses were performed on the same computer and under comparable conditions: the same mesh size, seismic-input duration (8 s), output sampling frequency (100 Hz), and output variables were adopted. The models with linear elements comprised 48,906 nodes (146,718 degrees of freedom), whereas the model with quadratic elements comprised 185,961 nodes (557,883 degrees of freedom). The output-file sizes are summarised in Table 6. The differences reflect the number of nodes and integration points associated with each element formulation. For large numerical models, computational time along with the volume and management of output data constitute an important practical consideration, particularly when conducting parametric studies or extensive sets of analyses.

Table 6. Output-file size.

Explicit Solver		**Implicit Solver**		
Linear elements		Linear elements		Quadratic elements
Full integration	Reduced integration	Full integration	Reduced integration	Full integration
3.12 GB	1.27 GB	4.67 GB	1.37GB	16 GB

The element formulation had no relevant influence on the displacement response, as all three implicit models produced results similar to those obtained with the explicit solver. However, this agreement was observed under predominantly elastic response and may not extend to severe nonlinear behaviour or near-collapse conditions. Since negligible damage developed, the implicit analyses did not exhibit significant convergence difficulties, which could otherwise increase the computational time or prevent the analyses from being completed. Therefore, an additional set of analyses was conducted using progressively increased amplitudes of the seismic input to evaluate the influence of the element formulation and time-integration method as the structural response became increasingly nonlinear.

Figure 15 presents the displacement time histories for seismic inputs with PGAs of 0.5 g and 0.9 g, together with the corresponding artificial energy ratios. All models over-

estimated the experimentally observed seismic capacity. At a PGA of 0.5 g, the responses remained predominantly elastic, although some residual deformation and moderate damage developed. Differences between the models began to appear as nonlinearities induced by damage became apparent. The models with reduced-integration elements produced nearly identical displacement time histories using the implicit and explicit solvers. The implicit model with linear reduced-integration elements employed the Stiffness hourglass-control formulation with s = 0.01, allowing direct comparison with the corresponding explicit model. These models with reduced integration elements exhibited a more flexible response than those with fully integrated elements once cracking developed at the corners. This difference became more pronounced at a PGA of 0.9 g, when the response exhibited stronger nonlinearities. Overall, the results suggest that the response was more sensitive to the element formulation than to the time-integration method. The reduced-integration models produced similar responses with both solvers at the different seismic-input amplitudes. Their responses differed from those of the models with fully integrated elements, which also showed similar displacement time histories to one another.

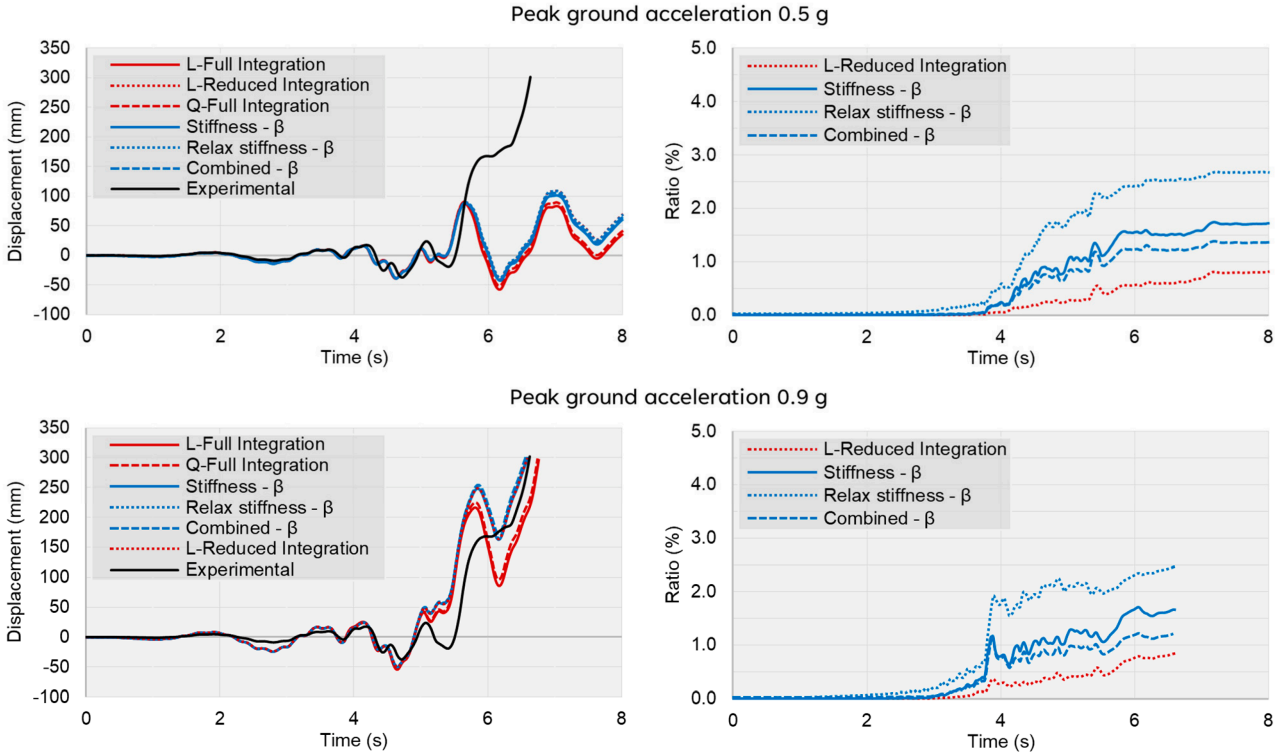


Figure 15. Response comparison between the implicit and explicit solvers for two increments of the PGA: 0.5 g and 0.9 g, along with the corresponding artificial energy ratios. Abbreviations indicate: L (linear element) and Q (quadratic element).

Regarding artificial energy, the results suggest that the 1% limit [34,51] may be more appropriate for the implicit analyses, whereas a higher threshold could be considered for the explicit analyses examined in this study, given the similar displacement responses obtained with both solvers but with higher artificial energy. Collapse in the explicit analyses occurred before the artificial energy ratio reached 3%. However, agreement between the displacement responses alone is insufficient to establish a generally applicable threshold.

The damping coefficient β limited the generation of artificial energy and resulted in deformation patterns and crack openings that more closely resembled the experimental observations, as shown in Figure 16. Nevertheless, β also strongly influenced the overall numerical response, leading to a substantial overestimation of the seismic capacity.

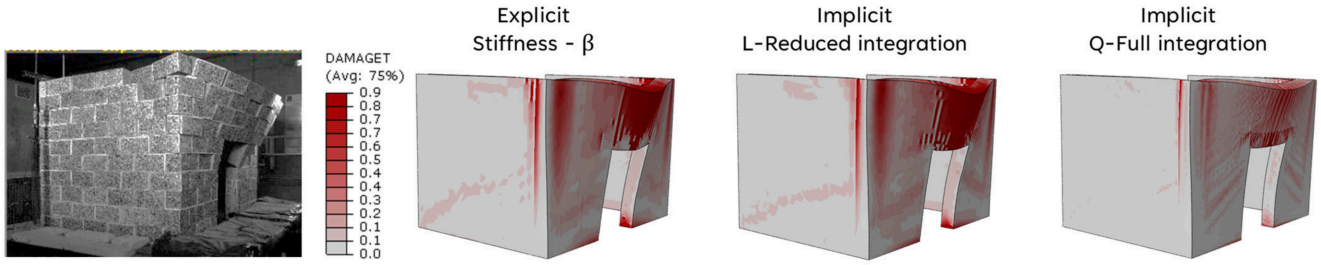


Figure 16. Deformation and damage patterns at a PGA of 0.9 g.

This behaviour can be explained by the frequency-dependent damping ratios defined by the Rayleigh formulation in Equation (9). Figure 17 shows the resulting curve for the models, obtained by assigning a damping ratio of ξ = 3% to Modes 1 and 11, the latter being the highest mode of interest. The curves corresponding to the individual contributions of α (blue) and β (red) are also shown. The experimental results indicated that collapse was governed by Mode 3. When only α was adopted, the damping ratio associated with this mode was ξ = 1.28%, whereas it increased to ξ = 2.24% when the contribution of β was added. Consequently, the higher damping ratio assigned to the mode governing collapse increased energy dissipation, leading to an overestimation of the dynamic capacity. Thus, the closer agreement between the experimental and numerical deformation patterns did not necessarily imply a more accurate prediction of the overall structural response. Given this sensitivity, further analyses should investigate the influence of the assumed damping ratio on the predicted response and collapse capacity.

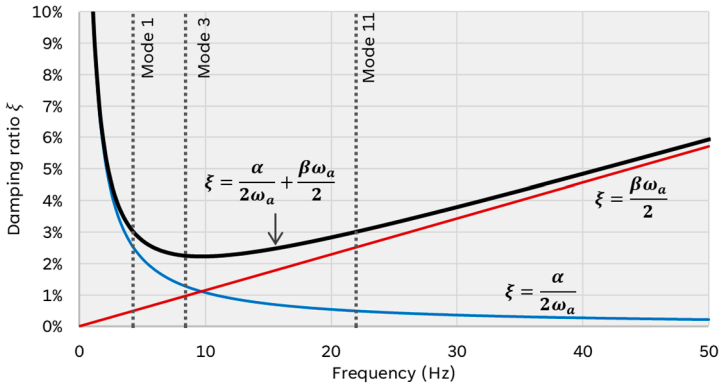


Figure 17. Rayleigh damping curve estimated for the models (α = 1.34957 s^{-1} and β = 0.000364 s).

The computational advantage of the explicit solver became more evident as nonlinear behaviour increased (Figure 18). At a PGA of 0.5 g, the explicit analyses required slightly less computational time than the implicit analyses. However, when collapse was reproduced, the implicit analyses required approximately twice the computational time of the corresponding explicit analyses. It should be recalled that the explicit models included in this comparison were composed of linear elements with reduced integration. It should also be noted that, for the implicit analyses, the linear models with full and reduced integration required similar computational times. Given that the models with reduced-integration elements produced nearly identical displacement responses with both time-integration methods, these results demonstrate the greater computational efficiency of the explicit solver for the large-displacement, strongly nonlinear response examined in this study.

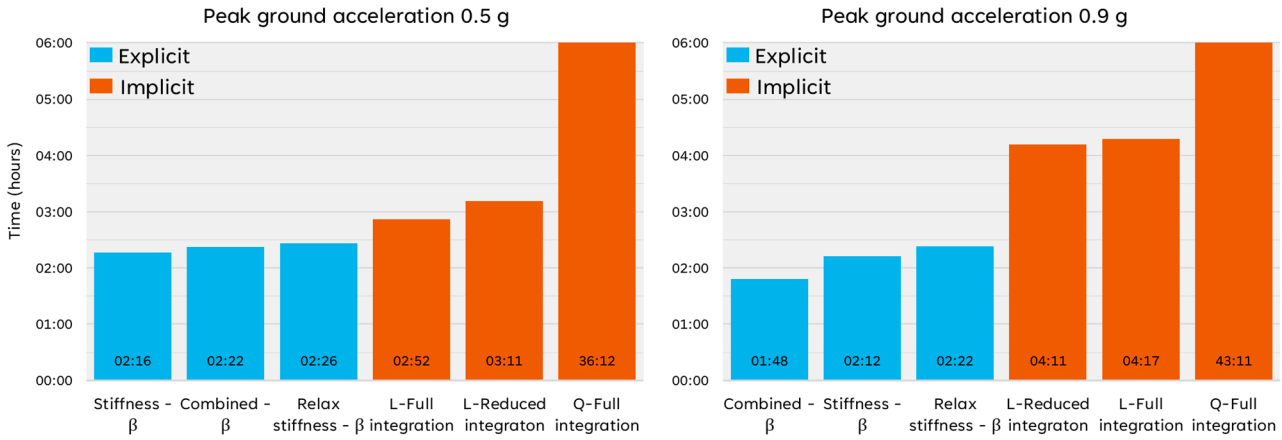


Figure 18. Computational time. Values within the bars indicate the computational time in hours and minutes (hh:mm).

The influence of the initial time increment on the implicit solution was also evaluated using the models with linear elements with full and reduced integration. Two additional analyses were conducted with an initial time increment of 0.0046 s, which corresponds to 1/10 of the period of Mode 11, as recommended in [61], and compared with the corresponding analyses using 0.002 s. Both increment sizes produced very similar displacement time histories and damage patterns. The analyses using 0.0046 s required 4h15min and 4h02min for the full- and reduced-integration models, respectively, corresponding to reductions in computational time of only 0.8% and 3.6%. Thus, increasing the initial time increment provided no substantial computational benefit.

7. Conclusions

The FEM simulation of highly nonlinear dynamic behaviour involves several interrelated challenges. Implicit methods allow relatively large time increments but require equilibrium iterations, which increase the computational cost and may lead to convergence difficulties as damage and large displacements develop. Explicit methods avoid these iterations but are conditionally stable and therefore require time increments below a critical value. Element formulation introduces an additional difficulty: linear elements with full integration may exhibit shear locking, whereas reduced integration can generate hourglass modes. Suppressing these modes requires artificial stabilising forces, which introduce artificial energy and may alter the response, leading to meaningless results.

This study investigated the influence of these numerical aspects on the nonlinear dynamic simulation of URM structures. The assessment considered the time-integration method, element formulation, hourglass-control parameters, artificial energy, and high-frequency damping, using the results of an experimental shake-table campaign as reference. The comparison focused on displacement response, collapse time, damage pattern, computational time, and output-file size.

A principal limitation of hourglass control is its dependence on an empirical, user-specified scale factor, which is sometimes troublesome. Insufficient control may allow spurious deformation modes, whereas excessive control may introduce artificial resistance and alter the structural response. This study assessed several hourglass-control formulations and scale-factor values to evaluate their influence on the response and artificial energy, providing preliminary guidance for nonlinear dynamic models of quasi-brittle materials, particularly URM.

Five hourglass-control formulations were selected to run nonlinear dynamic analyses, i.e., Relax stiffness, (pure) Stiffness, Combined (stiffness and viscous), Default (default

option in Abaqus), and Enhanced. Among them, Relax stiffness, Stiffness, and Combined hourglass-control formulations reproduced the global OOP collapse of the façade and produced similar tensile-damage patterns. Some differences were observed in the distribution and extent of damage, indicating the influence of the formulation adopted. However, none of the models reproduced the rotation of the upper corner units or the diagonal cracks observed experimentally in the sidewalls. These differences were mainly attributed to the homogenised continuum representation of the dry-joint masonry.

Before damage initiation, the hourglass-control formulations produced similar displacement responses. Their influence became evident when cracking and stiffness degradation began. For the formulations using Stiffness, Relax stiffness or Combined (a = 0.25, 0.50), increasing the scale factor s increased the stiffness of the numerical response and delayed collapse. This trend was not observed for the Combined formulation with a = 0.75, for which no clear relationship between s and displacement was identified.

Artificial energy increased after damage initiation because stiffness degradation and element distortion required a greater contribution from hourglass control. During the predominantly elastic response, the artificial energy ratio remained below 1% for the formulations using Stiffness or Relax stiffness and reached approximately 3.5% for the Combined formulations. During damage propagation, it generally remained between 5% and 7%, and several models reproduced collapse before reaching 10%. These results suggest that an artificial energy ratio of 5% may be used as a preliminary reference for predominantly elastic analyses, whereas values approaching 10% may still be compatible with simulations involving large deformations and collapse using the explicit solver. These values are not proposed as definitive limits and must be evaluated together with the structural response and energy balance, such as the Total energy ratio.

The damping parameters used to control the high-frequency response had a major influence on the results. Two values of the stiffness-proportional Rayleigh damping coefficient β were considered: the full calculated value and 10% of that value. Different values of the linear bulk viscosity parameter b were also evaluated as an alternative approach for introducing high-frequency damping. With the full value of β, the models remained predominantly elastic and did not predict the experimental collapse. A similar result was obtained with a linear bulk viscosity parameter of b = 5.0. Lower bulk viscosity values generally delayed collapse. The introduction of β also limited the generation of artificial energy. However, a lower artificial energy ratio did not indicate a more accurate solution, since β suppressed damage and altered the predicted collapse response.

The use of β produced deformation and damage patterns closer to those observed experimentally but substantially overestimated the seismic capacity. This occurred because β increased the damping assigned to the mode that governed the experimental OOP collapse. Therefore, agreement in deformation and damage alone was insufficient to validate the numerical response. Additionally, the full value of β and b = 5.0 also reduced the stable time increment by approximately a factor of seven, increasing the computational time.

Linear elements with full and reduced integration were considered with both the explicit and implicit solvers, whereas quadratic elements with full integration were evaluated only with the implicit solver. The element formulation had little influence when the models exhibited a predominantly elastic response. Once damage developed, the models with reduced integration elements produced a more flexible response than those with full integrated elements. However, for the same reduced integration formulation, the implicit and explicit solvers produced almost identical displacement responses. Thus, under the conditions analysed, the nonlinear response was more sensitive to the element formulation than to the time integration method.

The computational advantage of the explicit solver increased with the level of nonlinearity. The difference between the two solvers was small for predominantly elastic analyses. When models using the same element formulation were compared, the implicit solver required approximately twice as much computational time when collapse was simulated. Although this comparison is specific to the modelling and loading conditions adopted in this study, the findings suggest potential computational benefits when the explicit approach is applied. However, further investigation using larger and more complex models is required to confirm this potential advantage. The reduced-integration linear models also generated the smallest output files, approximately 1.3 GB, compared with 3.12–4.67 GB for the full integrated linear models and 16 GB for the quadratic model.

The findings are limited to the structural configuration, mesh, material model, and seismic input considered herein. In addition, the homogenised continuum approach cannot explicitly represent the opening and closing of dry joints or the rotation of individual masonry units. Further studies involving other masonry configurations, mesh discretisations, ground motions, damping ratios, and collapse mechanisms are required before the proposed artificial energy values and the other numerical observations can be generalised.

Author Contributions: Conceptualization, E.N.-M. and N.M.; methodology, E.N.-M. and N.M.; software, E.N.-M.; validation, N.M.; formal analysis, E.N.-M.; investigation, E.N.-M.; resources, N.M.; data curation, E.N.-M.; writing—original draft preparation, E.N.-M.; writing—review and editing, N.M.; visualization, E.N.-M.; supervision, N.M.; project administration, N.M.; funding acquisition, N.M. All authors have read and agreed to the published version of the manuscript.

Funding: This work was also supported by FCT/MCTES under the R&D Unit Institute for Sustainability and Innovation in Structural Engineering (ISISE), under the references UID/4029/2025 (https://doi.org/10.54499/UID/04029/2025), UID/PRR/04029/2025 (https://doi.org/10.54499/UID/PRR/04029/2025) and UID/PRR2/04029/2025 (https://doi.org/10.54499/UID/PRR2/04029/2025), and under the Associate Laboratory Advanced Production and Intelligent Systems ARISE under reference LA/P/0112/2020 (https://doi.org/10.54499/LA/P/0112/2020).

Data Availability Statement: The data presented in this study are available on request from the corresponding author.

Acknowledgments: The authors acknowledge Babar Ilyas and Moein Mirzaei, as well as the STAND4HERITAGE project (Grant No. 833123), for providing the shake-table experimental data.

Conflicts of Interest: The authors declare that they have no known competing financial interest or personal relationships that could have appeared to influence the work reported in this paper.

References

1. de Felice, G.; De Santis, S.; Lourenço, P.B.; Mendes, N. Methods and Challenges for the Seismic Assessment of Historic Masonry Structures. *Int. J. Archit. Herit.* **2017**, *11*, 143–160. [CrossRef]
2. D'Altri, A.M.; Sarhosis, V.; Milani, G.; Rots, J.; Cattari, S.; Lagomarsino, S.; Sacco, E.; Tralli, A.; Castellazzi, G.; de Miranda, S. Modeling Strategies for the Computational Analysis of Unreinforced Masonry Structures: Review and Classification. *Arch. Comput. Methods Eng.* **2020**, *27*, 1153–1185. [CrossRef]
3. Lourenço, P.B.; Gaetani, A. *Finite Element Analysis for Building Assessment; Advanced Use and Practical Recommendations*, 1st ed.; Routledge, Taylor & Francis Group: New York, NY, USA, 2022.
4. Karapitta, L.; Mouzakis, H.; Carydis, P. Explicit Finite-element Analysis for the In-plane Cyclic Behavior of Unreinforced Masonry Structures. *Earthq. Eng. Struct. Dyn.* **2011**, *40*, 175–193. [CrossRef]
5. Subbaraj, K.; Dokainish, M.A. A Survey of Direct Time-Integration Methods in Computational Structural Dynamics—II. Implicit Methods. *Comput. Struct.* **1989**, *32*, 1387–1401. [CrossRef]
6. Dokainish, M.A.; Subbaraj, K. A Survey of Direct Time-Integration Methods in Computational Structural Dynamics—I. Explicit Methods. *Comput. Struct.* **1989**, *32*, 1371–1386. [CrossRef]
7. Kim, W.; Lee, J.H. An Improved Explicit Time Integration Method for Linear and Nonlinear Structural Dynamics. *Comput. Struct.* **2018**, *206*, 42–53. [CrossRef]

8. Kim, W.; Reddy, J.N. Novel Explicit Time Integration Schemes for Efficient Transient Analyses of Structural Problems. *Int. J. Mech. Sci.* **2020**, *172*, 105429. [CrossRef]
9. Prior, A.M. Applications of Implicit and Explicit Finite Element Techniques to Metal Forming. *J. Mater. Process. Technol.* **1994**, *45*, 649–656. [CrossRef]
10. Noh, G.; Bathe, K.-J. An Explicit Time Integration Scheme for the Analysis of Wave Propagations. *Comput. Struct.* **2013**, *129*, 178–193. [CrossRef]
11. Pereira, J.M.; Campos, J.; Lourenço, P.B. Masonry Infill Walls under Blast Loading Using Confined Underwater Blast Wave Generators (WBWG). *Eng. Struct.* **2015**, *92*, 69–83. [CrossRef]
12. Pereira, J.M.; Lourenço, P.B. Risk Assessment Due to Terrorist Actions on Public Transportation Networks: A Case Study in Portugal. *Int. J. Prot. Struct.* **2014**, *5*, 391–415. [CrossRef]
13. Tse, D.; Pereira, J.M.; Lourenço, P.B. Numerical Analysis of an Earthen Masonry Structure Subjected to Blast Loading. *CivilEng* **2021**, *2*, 969–985. [CrossRef]
14. Al Sououb, D.; Salvalaggio, M.; Pereira, J.M.; Chalhoub, M.; Lourenço, P.B. Safeguarding Heritage Under Conflict: Numerical Investigation of the Blast Response of the Aleppo Citadel Minaret. *Heritage* **2026**, *9*, 101. [CrossRef]
15. Cundall, P.A. *UDEC—A Generalised Distinct Element Program for Modelling Jointed Rock*; U.S. Army European Research Office: Frankfurt, Germany, 1980.
16. Çaktı, E.; Saygılı, Ö.; Lemos, J.V.; Oliveira, C.S. Discrete Element Modeling of a Scaled Masonry Structure and Its Validation. *Eng. Struct.* **2016**, *126*, 224–236. [CrossRef]
17. Papantonopoulos, C.; Psycharis, I.N.; Papastamatiou, D.Y.; Lemos, J.V.; Mouzakis, H.P. Numerical Prediction of the Earthquake Response of Classical Columns Using the Distinct Element Method. *Earthq. Eng. Struct. Dyn.* **2002**, *31*, 1699–1717. [CrossRef]
18. Bui, T.T.; Limam, A.; Sarhosis, V.; Hjiaj, M. Discrete Element Modelling of the In-Plane and out-of-Plane Behaviour of Dry-Joint Masonry Wall Constructions. *Eng. Struct.* **2017**, *136*, 277–294. [CrossRef]
19. Lemos, J.V. Discrete Element Modeling of Masonry Structures. *Int. J. Archit. Herit.* **2007**, *1*, 190–213. [CrossRef]
20. Tóth, A.R.; Orbán, Z.; Bagi, K. Discrete Element Analysis of a Stone Masonry Arch. *Mech. Res. Commun.* **2009**, *36*, 469–480. [CrossRef]
21. Simon, J.; Bagi, K. Discrete Element Analysis of the Minimum Thickness of Oval Masonry Domes. *Int. J. Archit. Herit.* **2016**, *10*, 457–475. [CrossRef]
22. Lengyel, G. Discrete Element Analysis of Gothic Masonry Vaults for Self-Weight and Horizontal Support Displacement. *Eng. Struct.* **2017**, *148*, 195–209. [CrossRef]
23. Foti, D.; Vacca, V.; Facchini, I. DEM Modeling and Experimental Analysis of the Static Behavior of a Dry-Joints Masonry Cross Vaults. *Constr. Build. Mater.* **2018**, *170*, 111–120. [CrossRef]
24. Tarque, N.; Camata, G.; Spacone, E.; Varum, H.; Blondet, M. Nonlinear Dynamic Analysis of a Full-Scale Unreinforced Adobe Model. *Earthq. Spectra* **2014**, *30*, 1643–1661. [CrossRef]
25. Nochebuena-Mora, E.; Mendes, N.; Calixto, V.; Oliveira, S. Explicit Method in the Seismic Assessment of Unreinforced Masonry Buildings through Plane Stress Elements. *Appl. Sci.* **2023**, *13*, 10602. [CrossRef]
26. Yang, B. *Comparisons of Implicit and Explicit Time Integration Methods in Finite Element Analysis for Linear Elastic Material and Quasi-Brittle Material in Dynamic Problems*; Delft University of Technology: Delft, The Netherlands, 2019.
27. Noor-E-Khuda, S.; Dhanasekar, M.; Thambiratnam, D.P. An Explicit Finite Element Modelling Method for Masonry Walls under Out-of-Plane Loading. *Eng. Struct.* **2016**, *113*, 103–120. [CrossRef]
28. Olovsson, L.; Simonsson, K.; Unosson, M. Shear Locking Reduction in Eight-Noded Tri-Linear Solid Finite Elements. *Comput. Struct.* **2006**, *84*, 476–484. [CrossRef]
29. Caseiro, J.F.; Alves de Sousa, R.J.; Valente, R.A.F. A Systematic Development of EAS Three-Dimensional Finite Elements for the Alleviation of Locking Phenomena. *Finite Elem. Anal. Des.* **2013**, *73*, 30–41. [CrossRef]
30. Alves de Sousa, R.J.; Natal Jorge, R.M.; Fontes Valente, R.A.; César de Sá, J.M.A. A New Volumetric and Shear Locking-free 3D Enhanced Strain Element. *Eng. Comput.* **2003**, *20*, 896–925. [CrossRef]
31. Storheim, M.; Notaro, G.; Johansen, A.; Amdahl, J. Comparison of ABAQUS and LS-DYNA in Simulations of Ship Collisions. In Proceedings of the ICCGS, Ulsan, Republic of Korea, 15–18 June 2016.
32. Clough, R.W.; Penzien, J. *Dynamic of Structures*, 3rd ed.; Computers & Structures, Inc.: Berkeley, CA, USA, 2003.
33. Hilber, H.; Hughes, T.J.R.; Taylor, R.L. Improved Numerical Dissipation for Time Integration Algorithms in Structural Dynamics. *Earthq. Eng. Struct. Dyn.* **1977**, *5*, 283–292. [CrossRef]
34. Dassault Systèmes SIMULIA Corp. *Dassault Systèmes Abaqus Analysis User's Guide*, Version 6.14; Dassault Systèmes SIMULIA Corp: Providence, RI, USA, 2014.
35. Vecchio, D.; Ilyas, B.; Mendes, N.; Lourenço, P.B. Experimental Dynamic Out-of-Plane Response of Masonry Buildings: Mechanism Activation, Progression, and Collapse. *Eng. Struct.* **2026**, *365*, 123198. [CrossRef]
36. Autodesk Inc. *AutoCAD 2024*; Autodesk Inc.: San Francisco, CA, USA, 2023.

37. Dassault Systèmes Simulia Corp. *Abaqus/CAE 2025*; Dassault Systèmes Simulia Corp: Johnston, RI, USA, 2025.
38. Dassault Systèmes Simulia Corp. *Dassault Systèmes Theory Guide*, Version 6.14; Dassault Systèmes Simulia Corp: Johnston, RI, USA, 2014.
39. Nochebuena-Mora, E.; Mendes, N.; Lourenço, P.B. Seismic Analysis of Masonry Buildings Using Explicit Integration Method. In Proceedings of the 6as Jornadas Portuguesas de Engenharia de Estruturas, JPEE 2022, Lisbon, Portugal, 9–11 November 2022.
40. Vasconcelos, G.; Lourenço, P.B. Experimental Characterization of Stone Masonry in Shear and Compression. *Constr. Build. Mater.* **2009**, *23*, 3337–3345. [CrossRef]
41. D'Altri, A.M.; Cannizzaro, F.; Petracca, M.; Talledo, D.A. Nonlinear Modelling of the Seismic Response of Masonry Structures: Calibration Strategies. *Bull. Earthq. Eng.* **2022**, *20*, 1999–2043. [CrossRef]
42. Acito, M.; Bocciarelli, M.; Chesi, C.; Milani, G. Collapse of the Clock Tower in Finale Emilia after the May 2012 Emilia Romagna Earthquake Sequence: Numerical Insight. *Eng. Struct.* **2014**, *72*, 70–91. [CrossRef]
43. Tiberti, S.; Acito, M.; Milani, G. Comprehensive FE Numerical Insight into Finale Emilia Castle Behavior under 2012 Emilia Romagna Seismic Sequence: Damage Causes and Seismic Vulnerability Mitigation Hypothesis. *Eng. Struct.* **2016**, *117*, 397–421. [CrossRef]
44. Castellazzi, G.; D'Altri, A.M.; de Miranda, S.; Chiozzi, A.; Tralli, A. Numerical Insights on the Seismic Behavior of a Nonisolated Historical Masonry Tower. *Bull. Earthq. Eng.* **2017**, *16*, 933–961. [CrossRef]
45. Valente, M. Seismic Behavior and Damage Assessment of Two Historical Fortified Masonry Palaces with Corner Towers. *Eng. Fail. Anal.* **2022**, *134*, 106003. [CrossRef]
46. Valente, M. Earthquake Response and Damage Patterns Assessment of Two Historical Masonry Churches with Bell Tower. *Eng. Fail. Anal.* **2023**, *151*, 107418. [CrossRef]
47. Valente, M. Seismic Vulnerability Assessment and Earthquake Response of Slender Historical Masonry Bell Towers in South-East Lombardia. *Eng. Fail. Anal.* **2021**, *129*, 105656. [CrossRef]
48. Feenstra, P.H. *Computational Aspects of Biaxial Stress in Plain and Reinforced Concrete*; Delft University of Technology: Delf, The Netherlands, 1993.
49. Lubliner, J.; Oliver, J.; Oller, S.; Oñate, E. A Plastic-Damage Model for Concrete. *Int. J. Solids Struct.* **1989**, *25*, 299–326. [CrossRef]
50. AlGohi, B.H.; Baluch, M.H.; Rahman, M.K.; Al-Gadhib, A.H.; Demir, C. Plastic-Damage Modeling of Unreinforced Masonry Walls (URM) Subject to Lateral Loading. *Arab. J. Sci. Eng.* **2017**, *42*, 4201–4220. [CrossRef]
51. Boulbes, R.J. *Troubleshooting Finite-Element Modeling with Abaqus*; Springer International Publishing: Cham, Switzerland, 2020.
52. Puso, M.A. A Highly Efficient Enhanced Assumed Strain Physically Stabilized Hexahedral Element. *Int. J. Numer. Methods Eng.* **2000**, *49*, 1029–1064. [CrossRef]
53. Briassoulis, D. On the Basics of the Shear Locking Problem of C0 Isoparametric Plate Elements. *Comput. Struct.* **1989**, *33*, 169–185. [CrossRef]
54. Flanagan, D.P.; Belytschko, T. A Uniform Strain Hexahedron and Quadrilateral with Orthogonal Hourglass Control. *Int. J. Numer. Methods Eng.* **1981**, *17*, 679–706. [CrossRef]
55. Pian, T.H.H.; Chen, D. On the Suppression of Zero Energy Deformation Modes. *Int. J. Numer. Methods Eng.* **1983**, *19*, 1741–1752. [CrossRef]
56. Cheung, Y.K.; Changchun, W. A Study on the Stability of 3-Field Finite Elements by the Theory of Zero Energy Modes. *Int. J. Solids Struct.* **1992**, *29*, 215–229. [CrossRef]
57. Martin, O. *Comparison of Different Constitutive Models for Concrete in ABAQUS/Explicit for Missile Impact Analyses*; Publications Office of the European Union: Luxembourg, Luxembourg, 2010.
58. Zheng, G.; Nie, H.; Chen, J.; Chen, C.; Lee, H.P. Dynamic Analysis of Lunar Lander during Soft Landing Using Explicit Finite Element Method. *Acta Astronaut.* **2018**, *148*, 69–81. [CrossRef]
59. Belytschko, T.; Bindeman, L.P. Assumed Strain Stabilization of the Eight Node Hexahedral Element. *Comput. Methods Appl. Mech. Eng.* **1993**, *105*, 225–260. [CrossRef]
60. Belytschko, T. An Overview of Semidiscretization and Time Integration Procedures. In *Computational Methods for Transient Analysis*; Belytschko, T., Hughes, T., Eds.; Elsevier: New York, NY, USA, 1983; pp. 1–65.
61. Chopra, A.K. *Dynamics of Structures: Theory and Applications to Earthquake Engineering*, 4th ed.; Civil Engineering and Engineering Mechanics Series; Prentice Hall: Upper Saddle River, NJ, USA, 2012.
62. Hall, J.F. Problems Encountered from the Use (or Misuse) of Rayleigh Damping. *Earthq. Eng. Struct. Dyn.* **2006**, *35*, 525–545. [CrossRef]
63. Lemos, J.V.; Dawson, E.M.; Cheng, Z. Application of Maxwell Damping in the Dynamic Analysis of Masonry Structures with Discrete Elements. *Int. J. Mason. Res. Innov.* **2021**, *7*, 663–686. [CrossRef]
64. Chen, X.; Duan, J.; Qi, H.; Li, Y. Rayleigh Damping in Abaqus/Explicit Dynamic Analysis. *Appl. Mech. Mater.* **2014**, *627*, 288–294. [CrossRef]

65. Elmenshawi, A.; Sorour, M.; Mufti, A.; Jaeger, L.G.; Shrive, N. Damping Mechanisms and Damping Ratios in Vibrating Unreinforced Stone Masonry. *Eng. Struct.* **2010**, *32*, 3269–3278. [CrossRef]
66. Gonen, S.; Pulatsu, B.; Erduran, E.; Pelà, L.; Soyoz, S. Dynamic Characteristics of Stone Masonry Walls before and after Damage: Experimental and Numerical Investigations. *Eng. Struct.* **2024**, *306*, 117808. [CrossRef]
67. Mendes, N.; Lourenço, P.B. Sensitivity Analysis of the Seismic Performance of Existing Masonry Buildings. *Eng. Struct.* **2014**, *80*, 137–146. [CrossRef]
68. Sorrentino, L.; Masiani, R.; Griffith, M.C. The Vertical Spanning Strip Wall as a Coupled Rocking Rigid Body Assembly. *Struct. Eng. Mech.* **2008**, *29*, 433–453. [CrossRef]
69. Lagomarsino, S. Seismic Assessment of Rocking Masonry Structures. *Bull. Earthq. Eng.* **2015**, *13*, 97–128. [CrossRef]
70. Costa, A.A.; Penna, A.; Arêde, A.; Costa, A. Simulation of Masonry Out-of-plane Failure Modes by Multi-body Dynamics. *Earthq. Eng. Struct. Dyn.* **2015**, *44*, 2529–2549. [CrossRef]
71. Vlachakis, G.; Giouvanidis, A.I.; Mehrotra, A.; Lourenço, P.B. Numerical Block-Based Simulation of Rocking Structures Using a Novel Universal Viscous Damping Model. *J. Eng. Mech.* **2021**, *147*, 04021089. [CrossRef]
72. Luzi, L.; Lanzano, G.; Felicetta, C.; D'Amico, M.C.; Russo, E.; Sgobba, S.; Pacor, F. *ORFEUS Working Group 5: Engineering Strong Motion Database (ESM)*, Version 2.0; Istituto Nazionale Di Geofisica e Vulcanologia (INGV): Roma, Italy, 2020.
73. Ilyas, B.; Vecchio, D.; Mendes, N.; Lourenco, P.B. Shake Table Testing of U-Shaped Masonry Structures: Out-Of-Plane Response to Varying Ground Motion Signals. In Proceedings of the 3rd Croatian Conference on Earthquake Engineering-3CroCEE, Split, Croatia, 19–22 March 2025; pp. 467–479.

Disclaimer/Publisher's Note: The statements, opinions and data contained in all publications are solely those of the individual author(s) and contributor(s) and not of MDPI and/or the editor(s). MDPI and/or the editor(s) disclaim responsibility for any injury to people or property resulting from any ideas, methods, instructions or products referred to in the content.